Delft University of Technology

Computational prediction of underwater radiated noise of cavitating marine propellers
On the accuracy of semi-empirical models

Kalikatzarakis, Miltiadis; Coraddu, Andrea; Atlar, Mehmet; Gaggero, Stefano; Tani, Giorgio; Villa, Diego; Oneto, Luca

Important note
To cite this publication, please use the final published version (if applicable).
Please check the document version above.

Computational prediction of underwater radiated noise of cavitating marine propellers: On the accuracy of semi-empirical models

Miltiadis Kalikatzarakis [a], Andrea Coraddu [a,b,*], Mehmet Atlar [a], Stefano Gaggero [d], Giorgio Tani [d], Diego Villa [d], Luca Oneto [c]

[a] *Department of Naval Architecture, Ocean & Marine Engineering, University of Strathclyde, Glasgow, UK*
[b] *Department of Maritime & Transport Technology, Delft University of Technology, Delft, The Netherlands*
[c] *DITEN, Polytechnic School, University of Genoa, Genoa, Italy*
[d] *DIBRIS, University of Genova, Genova, Italy*

ARTICLE INFO

ABSTRACT

The potential impact of underwater radiated noise from maritime operations on marine fauna has become an important issue. The most dominant noise source on a propeller-driven vessel is propeller cavitation, producing both structure-borne and radiated noise, with a broad spectrum that covers a wide range of frequencies. To ensure acceptable noise levels for sustainable shipping, accurate prediction of the noise signature is essential, and procedures able to provide a reliable estimate of propeller cavitation noise are becoming a fundamental tool of the design process. In this work, we investigate the potential of using computationally cheap methods for the prediction of underwater radiated noise from cavitating marine propellers. We compare computational and experimental results on a subset of the Meridian standard propeller series, behind different severities of axial wake, for a total of 432 experiments. The results indicate that the approaches employed can be a convenient solution for noise analysis during the design process.

1. Introduction

1.1. Background

Underwater Radiated Noise (URN) has become a significant issue in the last few decades because of the substantial increase in shipping noise in oceans worldwide (Sezen et al., 2021c). Apart from considerations regarding crew and passenger comfort (Borelli et al., 2021; Ebrahimi et al., 2019; Sakamoto and Kamiirisa, 2018), research studies suggest that URN induced by the shipping sector in the frequency range between 10 Hz to 1 kHz is highly detrimental to the marine ecosystem (Erbe et al., 2019; Ferrier-Pagès et al., 2021; McKenna et al., 2017; Di Franco et al., 2020; Erbe et al., 2016; Popper and Hawkins, 2016). In this regard, several regulatory bodies have urged the industry to address the harmful effects of noise pollution (Williams et al., 2019; Ianniello et al., 2014b; Chou et al., 2021; Vakili et al., 2020a,b; Markus and Sánchez, 2018) and take precautionary measures (IMO, 2012, 2014; European Union, 2008, 2017a,b; Convention on Biological Diversity, 2014). Seagoing vessels have a very complex noise signature, consisting of rotating machinery noise, hydrodynamic flow noise due

to the turbulence in the boundary layer and the wake of the hull and appendages, and propeller radiated noise (Lurton, 2002). Among these sources, the propeller is the most significant contributor, generating the highest noise levels at frequencies below 200 Hz, a bandwidth which overlaps with the frequency band in the audible range of several marine mammals (Hildebrand, 2005, 2009). In addition, cavitation on the propeller blades significantly contributes to both tonal and broadband noise, with predominant noise levels ranging up to 1 MHz and dominating the overall URN spectrum above the inception threshold (Ross, 1976; Carlton, 2018).

For these reasons, significant effort has been devoted to the study and minimisation of propeller noise. In the past, the propeller design philosophy has always been to avoid cavitation for the widest possible range of operating conditions (Seol et al., 2005). However, recent demands for high-speed vessels and high propeller loads have rendered this design philosophy practically infeasible (Seol et al., 2005). To mitigate this issue, modern propeller designs incorporate multiple URN mitigation strategies: The increase of skewness that enables the propeller blade to pass through varying wakefields much more gradually,

therefore improving the cavitation pattern on the blades and increasing cavitation inception velocities (Da-Qing, 2006; Tong et al., 2021; Tong and Chen, 2020); forward-skewness, which makes the blade tip load less sensitive to changes of incidence compared to a straight-edged or backward-skew propeller, thus reducing the effects of varying inflow or vessel speed (Spence et al., 2007); the inclusion of an end plate in the propeller blade that enables a higher radial load distribution at the blade tip, thus reducing tip vortices and increasing cavitation inception speed (Gaggero et al., 2016b; Kim and Kinnas, 2021; Gaggero et al., 2016a); contra-rotating propeller systems that increase cavitation inception velocity by reducing blade load and blade surface cavitation, and also lower tip vortex cavitation by optimising the flow circulation around the propellers (Hu et al., 2019; Huang et al., 2019a,b; Nouri et al., 2018; Capone et al., 2021); the modification of the propeller tip, which is smoothly curved towards the suction side of the blades and is claimed to reduce tip vortices and increase cavitation inception velocity (Andersen et al., 2005, 2009).

Nevertheless, these strategies are usually conflicting with the requirement of high efficiency, and designers often resort to trade-off analyses that are case-specific and extremely time consuming (Gaggero et al., 2017a; Bertetta et al., 2012; Gaggero et al., 2017b, 2016b; Nouri et al., 2018; Vesting and Bensow, 2014; Valdenazzi et al., 2019). Furthermore, the effect of cavitation and its dynamics on URN is complex, and the current state of the art does not offer a plausible, physically-based URN prediction method that can be conveniently implemented within the propeller design process effectively (Aktas et al., 2016; Brooker and Humphrey, 2016; Ianniello et al., 2013, 2014a,b; Li et al., 2018). Experiments are time consuming and expensive, thus cannot be carried out for many different designs. Highly accurate numerical methods are not generally applicable in industry design processes, as they usually require substantial expertise and the coupling of multiple computational tools, which render them uneconomical and inefficient (Vesting and Bensow, 2014). For these reasons, the development of computational frameworks, providing highly accurate and cost-effective URN predictions and allowing for systematic variations on parametric propeller designs, becomes essential and imminent.

1.2. Related work

Computational tools for URN prediction can be divided in two main categories, characterised by different complexity and capability to model the underlying physics in Li et al. (2018): Empirical and semi-empirical models (Bosschers, 2018a, 2009; Brown, 1999; Bosschers, 2018c,b; Raestad, 1996; Lafeber and Bosschers, 2016; Lafeber et al., 2015; Bosschers, 2017; Wittekind and Schuster, 2016; Wittekind, 2014), and Computational Fluid Dynamics (CFD) methods.

Empirical and semi-empirical models were the first attempts in predicting cavitation noise and have been investigated by several researchers (Bosschers, 2018a, 2009; Brown, 1999; Bosschers, 2018c,b; Raestad, 1996; Lafeber and Bosschers, 2016; Lafeber et al., 2015; Bosschers, 2017; Wittekind and Schuster, 2016; Wittekind, 2014). Although these approaches model limited parts of the underlying physical phenomena, they are utilised extensively in the initial design stage due to their limited computational cost (Bosschers et al., 2017). Most simplified approaches for very initial predictions utilise fully-empirical formulas based on curve fitting to available measurement data. For instance, authors of Wittekind (2014) attempted to describe URN levels from propellers using geometric vessel parameters and simple algebraic equations, providing plausible qualitative trends. Empirical models for the broadband noise generated by cavitation was studied in Brown (1976), who proposed a simple equation to describe the upper limit of broadband noise in the frequency range between 100 Hz to 10 kHz based on measurements from thrusters. This idea has been further utilised and modified in several studies (Okamura and Asano, 1988; Ekinci et al., 2010; Takinacı and Taralp, 2013; Sakamoto and Kamiirisa, 2018), all of which reported satisfactory qualitative results in their

case studies. Authors of Brown (1999) presented a simple empirical formulation for the noise generated by thruster propellers. Their work provided a simple relation between the amplitude of noise and the area of sheet cavitation. Despite its lack of insight into the underlying physical phenomena, the method is known to predict the noise of open propellers with satisfactory results, as demonstrated in Lafeber and Bosschers (2016).

Semi-empirical models incorporate some theoretical considerations, typically consisting of different strategies for the tonal and broadband noise components. Tonal noise was studied in Okamura and Asano (1988), where a monopole model was used along with the lifting surface method (LSM) (Maines and Arndt, 1997) and the Rayleigh–Plesset equation (Brennen, 2014) to obtain the cavitation volume change.

Authors of Matusiak (1992) proposed a theoretical method to model the collapse of free bubbles due to sheet cavitation. The number and mean size of cavitation bubbles generated by a break-off of the unsteady sheet cavitation were modelled, and the URN levels were estimated using bubble dynamics. This idea was further adopted by Kamiirisa and Goto (2005) who estimated the behaviour of sheet cavitation using LSM and model tests, and introduced the effect of compressibility and damping in bubble flow to improve the prediction accuracy. Further improvements were later made in Ando et al. (1976), Lafeber et al. (2015) and Veikonheimo et al. (2016), where the same method was coupled to Reynolds-Averaged Navier–Stokes (RANS) or Boundary Element Method (BEM) simulations.

To deal with noise sources other than sheet cavitation, authors of Yamada and Kawakita (2015), Bosschers (2017, 2018c,b) and Raestad (1996) studied URN from tip vortex cavitation. More specifically, in Raestad (1996) the author formulated an empirical relation for the amplitude of vortex noise, whereas the author of Bosschers (2009) presented a formulation for the prediction of the characteristic frequency of noise generated by cavitating vortices. Both studies succeeded in approximating the behaviour of vortex noise. Nevertheless, they both require case-by-case tuning, as they rely on simplistic 2-dimensional vortex models (Bosschers, 2018a).

Authors of Yamada and Kawakita (2015) estimated propeller URN using the vortex strength estimated using LSM, and the vortex core size from boundary layer computations. With this information, the authors estimated bubble behaviour in the tip vortex cavity (TVC) and its noise utilising the Rayleigh–Plesset equation (Brennen, 2014) for bubble dynamics, and they combined their predictions with the broadband noise estimation method of Brown (1976), reporting satisfactory qualitative agreement with results from a higher fidelity RANS simulation. Authors of Kanemaru and Ando (2015) included a supercavitation model to the propeller tip region aiming to improve the accuracy of the higher order frequency fluctuations emitted from the tip vortices.

Authors of Bosschers (2017) combined their semi-empirical vortex model, which is a function of cavity size, propeller diameter, number of blades, and cavitation number, with BEM to predict the vortex cavity size, and used it to predict the hump-shaped pattern for the URN spectrum. Subsequently, their model was expanded and utilised in Bosschers (2018b,c), where the authors noted that the method is not able to model the phenomenon considering all possible dynamics, for instance the interactions with other phenomena if present.

More accurate results can be achieved with sophisticated CFD models, albeit at a higher computational cost. The commonly used approach involves the coupling of hydrodynamic solvers that detect the hydrodynamic sources of sound for cavitating propellers with the acoustic analogy (Sezen et al., 2021b). In this way, source and propagation fields can be decoupled: The source field is first determined by using the flow solver, whereas the propagation of the sound is provided by the aid of acoustic analogies from near field to far-field as a transfer function.

Depending on how various turbulence length scales are modelled or resolved, applied CFD methods can be classified as (Li et al., 2018): RANS or Unsteady RANS if the flow is treated as unsteady (Sezen et al., 2021c,b,a; Lee et al., 2021; Ge et al., 2020; Yao et al., 2021;

Melissaris et al., 2020; Wu et al., 2018; Peters et al., 2018; Huang et al., 2019b; Lidtke et al., 2019); Detached Eddy Simulations (DES) (Ku et al., 2021; Usta and Korkut, 2019; Long et al., 2021; Yilmaz et al., 2020; Sezen et al., 2021a; Sakamoto and Kamiirisa, 2018); and Large Eddy Simulations (LES) (Hu et al., 2019; Long et al., 2020; Hu et al., 2021; Asnaghi et al., 2020; Long et al., 2019; Asnaghi et al., 2018). The form of acoustic analogy mostly employed for the prediction of noise from moving bodies is based on the solution of the Ffowcs William-Hawkings (FWH) acoustic analogy formulation (Ffowcs Willams, 1969), which has proven to be an effective and reliable numerical tool for sound radiation problems dominated by fluid/body interactions (Brentner and Farassat, 2003; Farassat and Brentner, 1988). For this reason, it has been extensively used with different hydrodynamic solvers for the prediction of URN, under both cavitating and non-cavitating conditions (Bensow and Liefvendahl, 2016; Ianniello et al., 2013, 2014a,b; Kellett et al., 2013; Lidtke, 2017; Lloyd et al., 2015a,b, 2014; Seol et al., 2002, 2005; Sezen et al., 2021a; Testa et al., 2008). This method is essentially a rearrangement of the Navier–Stokes Equations for compressible flows, written in terms of a non-homogeneous wave equation where the forcing terms that account for the main sources of sound involve: the kinematics of the body; the unsteady pressure fluctuations on the body surfaces; and the flow-field sources described by the Lighthill Tensor (Bosschers et al., 2017). An extended body of literature has shown the feasibility of the method, and has underlined the main numerical issues and potential solutions (Bensow and Liefvendahl, 2016; Ianniello et al., 2013, 2014a,b; Kellett et al., 2013; Lidtke, 2017; Lloyd et al., 2015a,b, 2014; Seol et al., 2002, 2005; Sezen et al., 2021a; Testa et al., 2008).

For instance, authors of Testa et al. (2008) investigated the hydroacoustic performance of a marine propeller utilising FWH and a Bernoulli-based method, which were discussed primarily for naval applications. The authors showed that the FWH acoustic analogy was highly robust, and significantly outperformed the Bernoulli-based method.

Authors of Seol et al. (2002) conducted a numerical study for the prediction of non-cavitating propeller URN by utilising the FWH equation coupled with BEM, for a wide range of operating conditions. The aim of the study was to investigate the effects of duct geometry on overall URN, considering sound reflection and scattering effects. Satisfactory results were reported, and the study was further extended in Seol et al. (2005), where the authors studied URN levels and noise directivity patterns of each noise source under the presence of sheet cavitation on the DTMB4119 propeller, reporting good agreement with numerical results of previous studies.

More recently, authors of Ianniello et al. (2013) and Ianniello et al. (2014a) explored the non-cavitating hydroacoustic performance of the INSEAN E779A utilising RANS with different resolution forms of the FWH equation, i.e. impermeable and permeable, both in the isolated case and a complete vessel model. The authors concluded that URN is considerably affected by the contribution of nonlinear noise sources, and they must be included in the calculations for reliable predictions of propeller URN, regardless of propeller operational conditions. This study was further extended in Ianniello and De Bernardis (2015), where RANS and DES solvers were coupled with the FWH equation, with the authors concluding that RANS solvers were inadequate for hydroacoustics analyses.

The same approach was utilised in Lidtke et al. (2019) for the E779A propeller, with the aim to explore the crucial solution parameters for the prediction of URN. The authors concluded that larger porous data surface in the coarse grid region might risk information loss due to discretisation errors and dissipation.

The capabilities of FWH analogy were also demonstrated in Lloyd et al. (2014). The authors utilised a viscous CFD solver with porous FWH analogy for a two-bladed propeller model in open water conditions, demonstrating that the obtained results were in good agreement with their experimental data. An interesting comparison study was conducted in Testa et al. (2008), where the authors compared DES and BEM solvers coupled with a porous FWH equation for the E779A propeller under uniform and cavitating conditions. The authors concluded that the BEM solver was computationally cheap, yet inadequate to reflect the effects of non-linear noise sources as moving downstream of the propeller.

In summary, empirical and semi-empirical models have been extensively researched and comparisons between the prediction results and model or full-scale test results have shown acceptable qualitative agreement, with plausible trends (Bosschers, 2018a). Nevertheless, subsequent works that utilise the same empirical models often report discrepancies in the quality of the predictions obtained (Bosschers et al., 2017), demonstrating the need of case by case tuning of these methods to achieve acceptable accuracy.

On the other hand, the URN prediction by means of hybrid CFD methods is still a computationally expensive procedure, while also in this case achieving accurate and reliable results is not trivial.

1.3. Our proposal

In this work, we evaluate the capabilities of computationally cheap models for URN prediction that exhibit a favourable-trade off between the low-accuracy empirical models and the computationally expensive CFD numerical models. In particular, we investigate the potential of utilising a BEM to predict the pressure distribution on the surface of the propeller blades, along with the semi-empirical methods of Matusiak (1992) and Bosschers (2018c) to estimate the broadband effects of sheet cavitation, and the URN due to tip vortex cavitation, respectively. We carry out an extensive calibration process to derive appropriate values for all the parameters involved, ensuring that the models investigated commit the lowest possible error with respect to the available experimental data. To ensure the statistical consistency of the results, we test the proposed models in various interpolation and extrapolation scenarios that are typically encountered in practice, for which the calibration process is performed each time anew. We compare our computational results with 432 experiments performed in the Emerson Cavitation Tunnel (Aktas et al., 2016) on a small but commercially representative subset of the Meridian standard series propellers behind different wakefields. Furthermore, we also assess the ability of the models to predict URN levels on one additional propeller that is not part of the experimental dataset, having highly different geometry compared to the Meridian propellers. Results show that with careful selection of the associated parameter values, even computationally cheap semi-empirical models can provide highly accurate predictions in a cost-effective manner, making them especially convenient for use in a conventional propeller design loop.

The rest of the paper is organised as follows. Section 2 details the experimental data used in this work. Section 3 discusses the numerical methods used to evaluate flow features and the URN for the considered propellers and wake fields. Section 4 discusses the process of estimating the parameters of the methods described in Section 3. Section 5 reports comparative results between the numerical methods and the experimental data, and Section 6 underlines the most important conclusions of this work.

2. Available data

For the scope of this work, we utilise the dataset generated in the extensive measurement campaign of Aktas (2017) and Aktas et al. (2018). In these studies, the authors conducted systematic cavitation tunnel tests at the Emerson Cavitation Tunnel of Newcastle University (Atlar, 2011), with 6 members of the Meridian Standard propeller series (Emerson, 1978) and 3 wakefields. With these propellers and wakefields, the authors conducted a full factorial experimental design with a constant inflow velocity of 3 m/s, including 3 different levels of
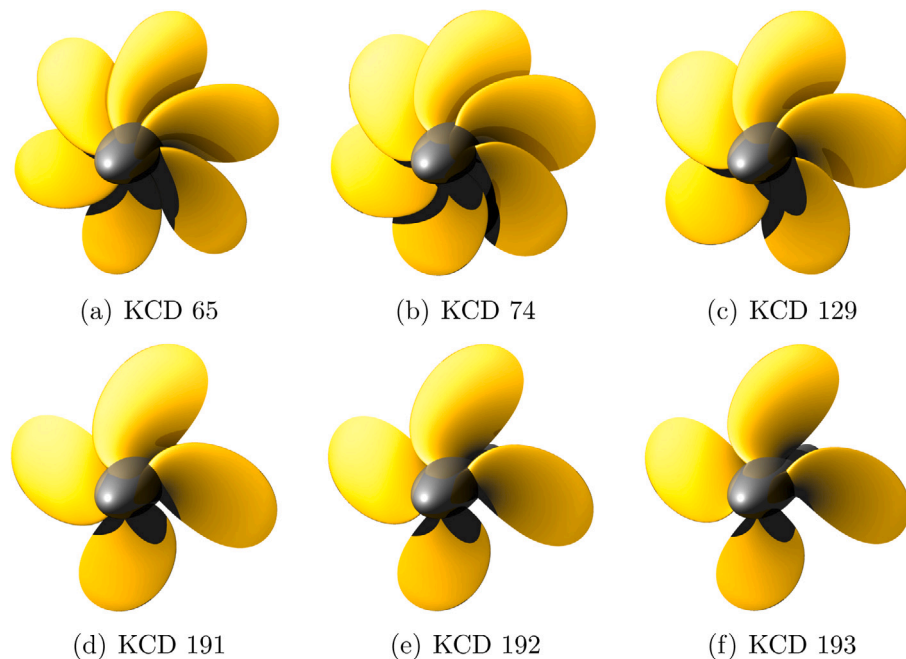
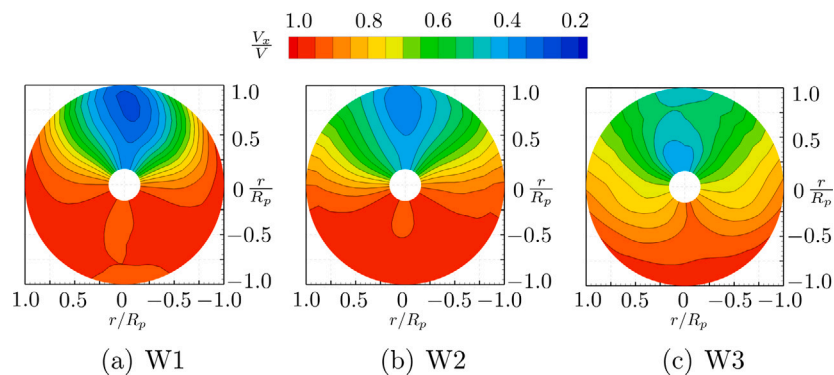**Fig. 1.** Visual impression of the propellers in the dataset.

Fig. 2. Contour plots of axial velocity distributions of the wakefields in the dataset.

tunnel vacuum conditions (atmospheric, 150 mmHg, 300 mmHg) and 8 propeller rotational speeds for a total of 432 experiments.

The Meridian propeller series, derived from the proprietary propeller design of Stone Manganese Marine Ltd., is a unique standard series based solely on practical propeller designs with standardised variations in pitch-to-diameter ratio (P/D), blade area ratio (A_E/A_O) and number of blades. Initially, the series comprised 4 parent models having a combination of 4 distinct blade area ratios $A_E/A_O \in \{0.45, 0.65, 0.85, 1.05\}$, and 5 mean pitch-to-diameter ratios $P/D \in \{0.4, 0.6, 0.8, 1.0, 1.2\}$. All the models have a diameter D of 304.8 mm and $Z = 6$ blades, with a hub diameter $D_h = 0.185 \times D$. Currently there are 60 propellers in the series, with $Z \in \{4, 5, 6\}$, $A_E/A_O \in [0.45 - 1.05]$ and $P/D \in [0.4 - 1.2]$ (Carlton, 2018). The subset utilised in this work includes the propeller models: KCD 65, KCD 74, KCD 129, KCD 191, KCD 192, and KCD 193, presented in Fig. 1.

The authors of Aktas (2017) and Aktas et al. (2018) selected the wakefields based on the criteria suggested by Konno et al. (2002), Angelopoulos et al. (1988) and Odabasi and Fitzsimmons (1978). According to these studies, wakefields with steeper velocity changes produce higher tonal amplitudes of pressure fluctuations, as well as high-frequency contributions from increased dynamic cavity collapses, both away from and on the blade surface. Based on these observations, the wake non-uniformity, mean wake, half- wake width and wake depth were controlled to generate 3 wakefields, referred to as W1, W2, and W3, that will induce variation in the inflow velocities of varying severity. These changes will subsequently induce the formation of unsteady cavitation from the collapse and rebound of cavity volumes at the exit of the wake peak region. Fig. 2 provides a visual impression of these wakefields.

In the experiments conducted, the URN was measured by one hydrophone placed in the tunnel test section, and was acquired in the form of pressure time traces. These time-traces were subsequently converted in 1/3 octave band, corrected for background noise, and converted to the standard measuring distance of 1 m according to the recommendations of ITTC (2017). A visual impression of the experimental setup is presented in Fig. 3, whereas Table 1 lists the full set of quantities collected from these experiments.

To provide a visual impression of the operating conditions covered in the dataset, Figs. 4–5 report the open water diagrams, operating points and cavitation indices (based on rotational speed at the blade tip) of all the propellers in the dataset. As can be seen, the dataset covers a broad operating region for all propellers, with $J \in [0.3 - 0.8][-]$ and $\sigma_{n,tip} \in [0.15, 1.4]$ for propellers KCD 65, KCD 74, KCD 129, and KCD 191, and $J \in [0.3 - 1.0][-]$, $\sigma_{n,tip} \in [0.25, 2.2]$ for propellers KCD 192, and KCD 193.

Finally, Fig. 6 provides a visual impression of the additional propeller utilised strictly to assess the prediction capabilities using the
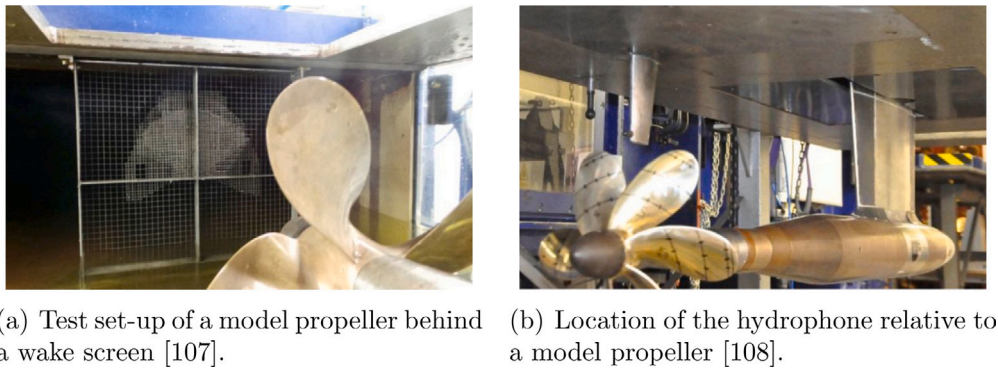
(a) Test set-up of a model propeller behind a wake screen [107].

(b) Location of the hydrophone relative to a model propeller [108].

Fig. 3. Experimental setup.

(a) KCD 65

(b) KCD 74

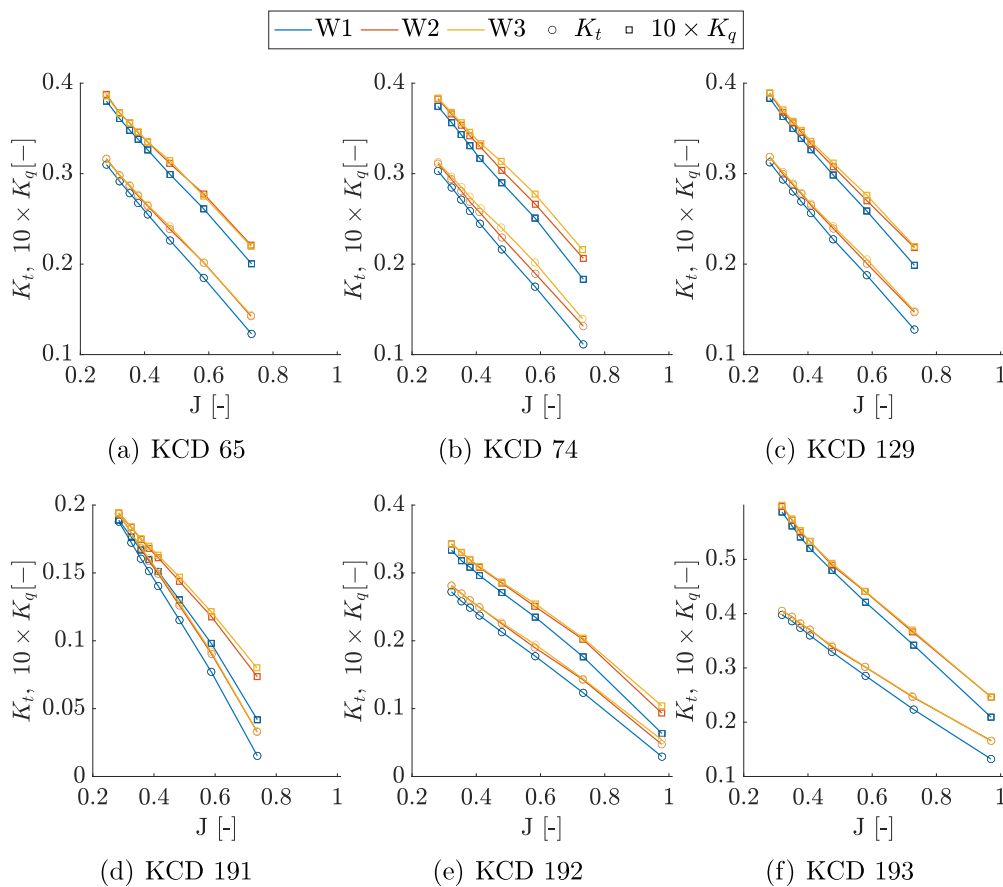(c) KCD 129

(d) KCD 191

(e) KCD 192

(f) KCD 193

Fig. 4. Operating points of the propellers in the dataset.

models of Section 3. Compared to the Meridian propellers initially employed for the calibration of the semi-empirical URN models, this geometry has a rather modern design having a skew at tip greater than 40 deg. The functioning point defines this geometry as a moderately loaded propeller since it was designed for a semi-displacement small passenger ship (reference displacement of 60 tons) operating at a design speed of 20 knots. In these conditions, the cavitation index is about equal to 1.4 and it is lower than 1.2 at the maximum ship speed of 25 knots. These characteristics, which indicate serious risk of sheet and tip vortex cavitation, together with the possible operation of the ship in restricted areas, made this propeller the ideal candidate for detailed numerical and experimental analyses that were carried out in the framework of the EU funded project PIAQUO (LIFE-PIAQUO, 2021) specifically devoted to ship noise prediction and mitigation. In this context, the experimental measurements were made available by

the cavitation tunnel of the University of Genoa, following the same standard procedure (pressure time traces converted to 1 m distance) used to process the signals of the Meridian series propellers. Usual propeller performance and high-speed visualisation of the cavitation process revealed the expected cavitation of the tip vortex and the occurrence of both suction and pressure side sheet cavitation, making this geometry a challenging test case for the semi-empirical models under investigation.

3. Numerical methods

In this section, we give an overview of the numerical models utilised to compute the URN spectra that will be compared with experimental measurements in Section 5. These models include a BEM for the computation of the hydrodynamic performance of the propeller models, the
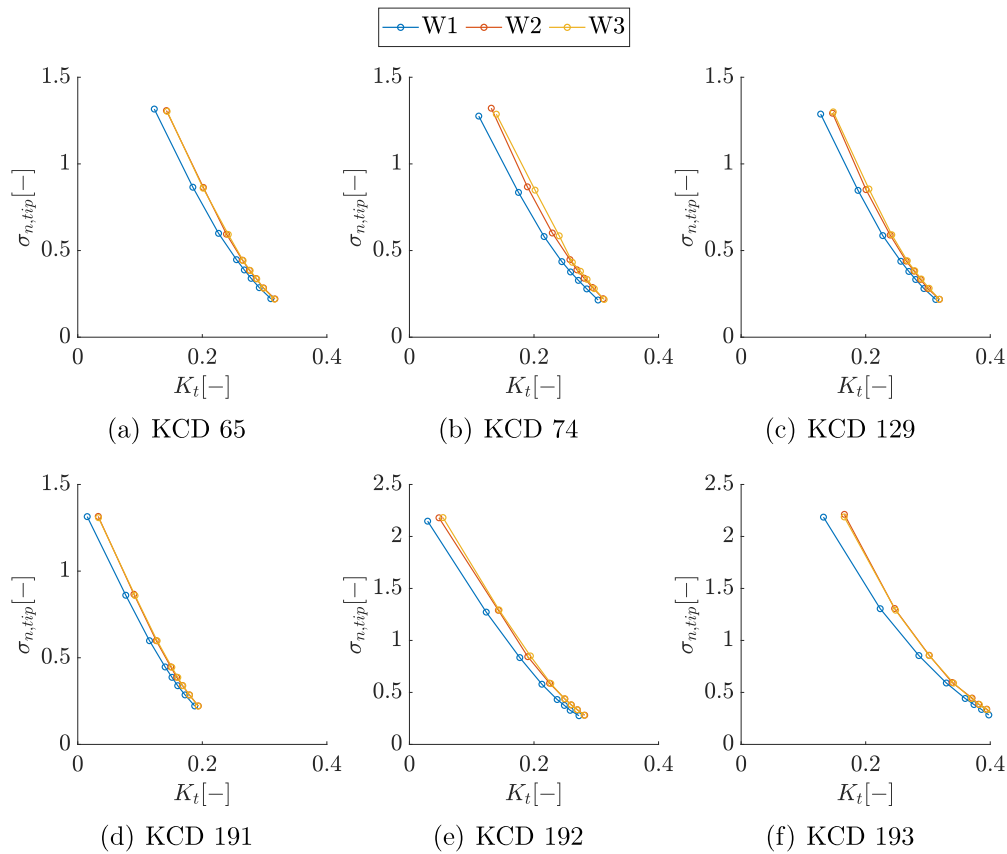
(a) KCD 65 (b) KCD 74 (c) KCD 129

(d) KCD 191 (e) KCD 192 (f) KCD 193

Fig. 5. Cavitation indices of the experiments in the dataset.

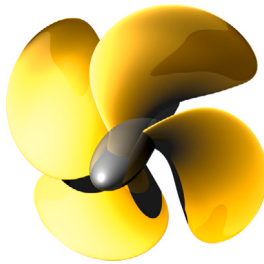**Fig. 6.** Visual impression of the additional propeller scale model utilised to test the performance of the numerical methods.

Table 1
Quantities available in the dataset.

Symbol	Description	Size[a]	Units
Propeller geometry			
D	Propeller diameter		m
Z	Number of blades		–
A_E/A_O	Blade aspect ratio		–
p	Sectional pitch ratio	1×8	–
c	Sectional chord ratio	1×8	–
i_T	Sectional total rake ratio	1×8	–
t_{max}	Max. sectional thickness ratio	1×8	–
f_{max}	Max. sectional camber ratio	1×8	–
θ_s	Sectional skew angle	1×8	deg
Operating conditions			
n_p	Propeller rotational speed		rpm
V_a	Advance velocity		m/s
p_{rel}	Tunnel pressure relative to ambient pressure		mbar
w_t	Axial wakefield	22×60	–
J	Advance coefficient		–
K_t	Thrust coefficient		–
$10K_q$	Torque coefficient		–
η_o	Propeller efficiency		–
σ_n	Cavitation index ref. on rotational speed		–
f	Frequency vector for the correspondent RNL	1×31	Hz
RNL	Radiated noise levels in 1/3 octave band	1×31	dB

[a] Empty field indicates scalar quantity.

semi-empirical model of Matusiak (1992) to estimate URN induced by sheet cavitation, referred to as the "Matusiak model", and the semi-empirical ETV model (Bosschers, 2018a,c) for the estimation of URN due to TVC.

3.1. Boundary element method

We performed unsteady hydrodynamic computations by means of an in-house developed BEM code that provides an accurate characterisation of the hydrodynamic field of the propeller at an acceptable computational cost (Gaggero et al., 2010, 2014; Bertetta et al., 2012; Gaggero and Villa, 2018). The developed numerical code has been verified for a variety of propeller types, including supercavitating (Gaggero and Brizzolara, 2009), ducted (Gaggero et al., 2013), and tip loaded propellers (Gaggero et al., 2016b), and for cavitating flows in both steady (Gaggero and Villa, 2017) and unsteady conditions (Gaggero and Villa, 2018), for strongly non-homogeneous wakefields in Gaggero

et al. (2010, 2014), and for very off-design conditions in Gaggero et al. (2019).

BEM models the flow field around a solid body using a scalar function, the perturbation potential ϕ, whose spatial derivatives represent the perturbation velocity vector components. Assuming irrotationality, incompressibility, and the absence of viscosity allows to express the continuity equation as a Laplace equation for the perturbation potential
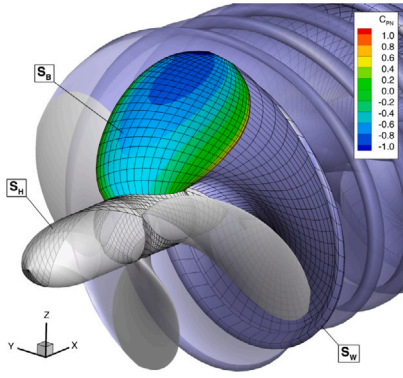
Fig. 7. Mesh arrangement on the propeller surface and resulting pressure coefficient. KCD 192 in steady flow, $J = 0.6$.

as follows:

$$\nabla^2 \phi(\boldsymbol{x}, t) = 0 \tag{1}$$

Green's third identity allows to solve the three dimensional differential problem as a simpler integral problem written only for the surfaces that bound the domain. In the context of non-cavitating flows, these surfaces include the fully wetted surface of the blades (S_B) and of the hub (S_H) plus the trailing wake surface S_W. The latter refers to the zero thickness layer, which departs at the trailing edge of the lifting surfaces, where vorticity is shed onto the downstream flow, as shown in Fig. 7. The solution is obtained as the intensity of a series of mathematical singularities distributed on the boundaries (i.e. dipoles $-\phi$ and sources $\frac{\partial \phi}{\partial n}$) which superposition models the perturbation potential and then the inviscid flow in the entire computational domain (Morino and Kuo, 1974):

$$2\pi\phi(\tilde{\boldsymbol{x}}, t) = \int_{S_W} \Delta\phi_W(\boldsymbol{x}, t) \frac{\partial}{\partial \boldsymbol{n}} \frac{1}{r} dS +$$
$$+ \int_{S_B + S_H} \phi(\boldsymbol{x}, t) \frac{\partial}{\partial \boldsymbol{n}} \frac{1}{r} dS - \int_{S_B + S_H} \frac{\partial \phi(\boldsymbol{x}, t)}{\partial \boldsymbol{n}} \frac{1}{r} dS, \tag{2}$$

where $\boldsymbol{n}$ is the unit normal, r is the distance between points $\tilde{\boldsymbol{x}}$ and $\boldsymbol{x}$, and Δ denotes the potential jump (i.e., the net dipole intensity) across the wake surface. The pressure forces, once the potentials/velocities are defined, can be computed by applying the unsteady formulation of Bernoulli's theorem.

The numerical solution consists of an inner iterative scheme that solves the non-linearities related to the Kutta condition at the blade trailing edge and an outer iterative cycle to integrate over time by shedding in the wake the correct amount of vorticity in accordance with the Kelvin theorem. To this aim, the *key blade* approach proposed by Hsin (1990) is exploited: only one blade (plus its wake and portion of the hub) is solved while the influence of other blades is accounted iteratively during propeller revolutions until a periodic solution after the numerical transient is achieved.

In current analyses, we use a surface mesh for the key blade of 1000 panels plus 360 on the hub. The trailing vortical wake extends for eight revolutions with a spatial discretisation corresponding to an equivalent time step of 6 deg.

3.2. Broadband effects of sheet cavitation

The Matusiak model assumes that any change in the volume rate of the generated bubbles equals the rate at which the sheet cavity volume decreases:

$$\frac{d}{dt}\left(\sum_{i=1}^{n_b} V_i\right) = \frac{d}{dt}\left(n_b \bar{V}\right) = \begin{cases} -\beta_f \frac{d}{dt}\left(A_c\right) dr, & \text{for } \frac{d}{dt}\left(A_c\right) < 0 \\ 0, & \text{for } \frac{d}{dt}\left(A_c\right) \geq 0 \end{cases} \tag{3}$$

where V_i is the volume on the ith bubble, n_b is the total number of bubbles generated during one time-step, β_f corresponds to the gas/vapour fraction, dr is the blade span differential, and A_c refers to the cavitating area in a cross section of the blade. The latter is estimated according to the method of Geurst (1961) from the unsteady pressure distributions computed with BEM.

The average bubble volume $\bar{V}_b$ is defined on the basis of the size distribution of the bubbles f_b, which is assumed to be a beta distribution of the form

$$f_b(r_b) = m(1 - r_b)^{m-1}, \quad r_b = \frac{2R_b}{\eta_c}, \quad \eta_c = c_b \frac{A_c}{L_c}, \tag{4}$$

where m is a constant, r_b is the non-dimensional bubble radius, R_b refers to the radius of each bubble, η_c is the (fixed) cavity thickness at the point of break-off, L_c refers to the cavity length, and c_b is a calibration constant.

The volume distribution of the bubbles is obtained from Eq. (4), considering that $v_b(r_b) = 4/3\pi r_b^3$ as

$$f_v(r_b) = f_b(r_b) \frac{dr_b}{dv} = \frac{m}{4\pi} \frac{(1 - r_b)^{m-1}}{r_b^2}, \tag{5}$$

with the mean bubble volume being

$$\bar{V}_b = \left(\frac{\eta_c}{2}\right)^3 \bar{v}_b, \quad \bar{v}_b = \int_0^{v(1)} v f_v(v) dv. \tag{6}$$

Assuming that $\bar{V}_b$ remains constant within one time-step (Δt), we can compute the total number of bubbles Δn_b generated for blade length dr as

$$\Delta n_b = -\frac{\beta_f}{\bar{V}_b} \left[A_c(t + \Delta t) - A_c(t)\right] dr. \tag{7}$$

The newly-generated bubbles are transported towards the trailing edge at the local speed of the flow $U(r, \theta, t)$, and the blade pressure is assumed to increase monotonically from the vapour pressure p_v, to the static pressure p_0 at the trailing edge. Under the assumption of linear pressure growth, the ambient pressure at the location of the bubble can be approximated as

$$p_\infty(t) = p_v + \frac{t}{t^*}(p_0 - p_v), \tag{8}$$

with $t^* = (v_s - L_c)/U$ being the bubble travelling time to the trailing edge, and v_s being the local sound velocity.

This computation is performed for every time-step and for all radial sections of the key blade. If the local cavity is shrinking, i.e., a bubble cloud is generated, the total number of cavitation bubbles and their mean volume are evaluated and discretised into a number of bubble classes n_b. To compute the pressure trace generated by each bubble class, a bubble dynamics equation must be integrated over time. From all approaches that can be utilised to describe the oscillations of radially symmetric bubbles (Brennen, 2014) we employ the Gilmore equation (Gilmore, 1952), given by

$$\left(1 - \frac{\dot{R}_b}{c_g}\right) R_b \ddot{R}_b + \frac{3}{2}\left(1 - \frac{\dot{R}_b}{3c_g}\right) \dot{R}_b^2 = \left(1 + \frac{\dot{R}_b}{c_g}\right) H_b + \left(1 - \frac{\dot{R}_b}{c_g}\right) \frac{R_b}{c_g} \dot{H}_b. \tag{9}$$

Assuming isentropic compression and linearly increasing pressure, the terms H_b, $\dot{H}_b$ and c_g are evaluated as

$$H_b = \frac{n_T}{\rho} \frac{p_\infty + B_T}{n_T - 1}\left[\left(\frac{p_{bi} + B_T}{p_\infty + B_T}\right)^{\frac{n_T - 1}{n_T}} - 1\right], \tag{10}$$

$$c_g = c_{g0}\left[\frac{p_v + p_{g0}\left(\frac{R_{b,0}}{R_b}\right)^{3k} - 2\frac{\sigma}{R_b} + B_T}{p_\infty(t) + B_T}\right]^{\frac{n_T - 1}{2n_T}}, \tag{11}$$

$$\dot{H}_b = \frac{p_w H_b}{p_v + p_w t + B} - \frac{p_w}{\rho}\left(\frac{p_{bi} + B_T}{p_v + p_w t + B_T}\right)^{\frac{n_T - 1}{n_T}} +$$

Table 2
Constants of Gilmore equation (Gilmore, 1952).

Parameter	Symbol	Value (Matusiak, 1992)	Units
Polytropic index	k	1.4	[–]
Bulk constant	B_T	3×10^8	[Pa]
Bulk constant	n_T	7	[–]
Vapour pressure	p_v	857	[Pa]
Initial gas pressure	p_{g0}	857	[Pa]
Surface tension	σ	0.0725	[N/m]

Table 3
Parameter set S of the semi-empirical models.

Method	Symbol	Equation	Value[a]	Symbol	Equation	Value[a]
Matusiak model (Section 3.2)	β_f	Eq. (3)	0.8	m	Eq. (4)	9
	n_b	Eq. (3)	5	c_b	Eq. (4)	1.8
	τ_b	Eq. (10)	3.5			
ETV model (Section 3.3)	ζ_3	Eq. (13)	10	Δf_{-6dB}	Eq. (14)	–
	a_l	Eq. (15)	4	a_h	Eq. (15)	−2
	τ	Eq. (16)	–	α_s	Eq. (17)	0.8
	a_p	Eq. (18)	–			

[a] [–] indicates that the constant has no recommended value, implying that a curve-fitting procedure must be used.

Table 4
Bounded space of S used during the calibration process.

Method	Symbol	$s_{\min}$	$s_{\max}$	Symbol	$s_{\min}$	$s_{\max}$
Matusiak model (Section 3.2)	β_f	0.1	1.0	m	1	9
	n_b	2	500	c_b	0.6	3.0
	τ_b	2	350			
ETV model (Section 3.3)	ζ_3	−0.1	0.6	Δf_{-6dB}	5	15
	a_l	1	10	a_h	−10	−1
	τ	0.6	1.4	α_s	0	1
	a_p	50	150			

$$+ \frac{\dot{R}_b}{\rho R_b} \left(\frac{p_v + p_w t + B_T}{p_{bi} + B_T} \right)^{\frac{1}{n_T}} \left[\frac{2\sigma}{R_b} - 3k p_{g0} \left(\frac{R_{b,0}}{R_b} \right)^{3k} \right], \tag{12}$$

where n_T and B_T are the constants of Tait's law of compressibility, p_{g0} is the initial gas pressure, k is the polytropic index, σ is the surface tension coefficient, and the symbol p_{bi} is used for the internal bubble pressure. The subscript 0 refers to initial values within the current time-step, and $p_w = \frac{p_0 - p_v}{t^*}$ describes the linearly increasing pressure on the liquid side of the bubble wall. The constants used in the Gilmore equation are given in Table 2.

The Gilmore equation is solved for a fixed number of oscillations τ_b. The time-traces obtained are offset by a random, uniformly distributed time lag within the current time-step, with the assumption that the initial gas pressure in the bubble is equal to the vapour pressure as suggested in Matusiak (1992). We apply this procedure to every bubble in each bubble class and for all classes, with the summation of all time traces forming the total field pressure. Subsequently, the Fourier Transformation of the total field pressure is evaluated, yielding the complex pressure spectrum from which we obtain the URN spectra.

3.3. Tip vortex induced noise

ETV is a semi-empirical model, based on the Tip Vortex Index (TVI) method (Raestad, 1996). TVI relates the measured URN to the predicted size of the vortex cavity, using a computed circulation distribution on the propeller blade. The ETV model follows a similar approach, but it predicts the broadband spectrum of URN slightly differently. It is composed by two sub-models:

- The vortex model that describes the tangential velocity of the vortex given a measure of the vortex strength,
- The model that represents the relation between the vortex cavitating radius r_c and its characteristic noise.

To compute the frequency and noise amplitude due to vortex pulsation, the cavity radius, which is defined as the radial distance r from the vortex axis, has to be estimated. This estimation requires the use of a vortex model. Among the several vortex models available in the literature (Franc and Michel, 2006) we utilise the Proctor vortex model (Saffman, 1992). This model assumes constant axial velocity, which occurs on two-dimensional and axisymmetric flows, negligible radial velocity with respect to the tangential velocity, and constant velocity distribution in the azimuthal direction. Under these assumptions, the azimuthal velocity $v_\theta(r)$ is given by

$$v_\theta(r) = \begin{cases} 1.0939 \frac{\Gamma_\infty}{2\pi r} \left[1 - e^{-\zeta_3 \left(\frac{1.4 r_v}{D/2} \right)^{\zeta_2}} \right] \left[1 - e^{-\zeta_1 \left(\frac{r}{r_v} \right)^2} \right] & \text{for } r \leq 1.4 r_v \\ \frac{\Gamma_\infty}{2\pi r} \left(1 - e^{-\zeta_3 \left(\frac{r}{D/2} \right)^{\zeta_2}} \right) & \text{for } r > 1.4 r_v \end{cases} \tag{13}$$

where r_v is the size of the viscous core, and Γ_∞ is the vortex strength for the tip blade section. $\zeta_1 = 1.26$, $\zeta_2 = 0.75$ as suggested in Proctor et al. (2010), and ζ_3 is a calibration constant, which was set equal to 10 in Proctor et al. (2010).

Regarding r_v, it is an input which may differ for every propeller and functioning condition. Since direct measurements are not available for the present cases, we utilise reference values from Jessup (1989), scaled according to the procedure proposed in Shen et al. (2009) to account for the different Reynolds numbers. This scaling provides a first reasonable estimate of the viscous core. Nevertheless, we adjust the obtained values utilising a constant multiplication factor as suggested in Bosschers (2018c). With the known azimuthal velocity distribution, we obtain the pressure distribution by integrating the momentum equation in the radial direction (Hommes et al., 2015). This process provides a relation between cavity radius and cavitation number, from which the r_c can be estimated. Subsequently, the cavity radius is used to estimate the source level spectrum, which is divided in two frequency parts:

- The part H_h that is characterised by a hump around the resonance frequency of the vortex cavity f_c, due to the overall growth, collapse and rebounds of the cavity, given by

$$H_h(f) = 20 \log_{10} \left[sinc \left(\frac{f - f_c}{\Delta f_{-6dB}} \right) \right], \tag{14}$$

- and the part H_s related to the final phase of the cavity collapse process, which consists of prescribed slopes at frequencies much lower and much higher than the resonance frequency, computed as

$$H_s(f) = 10 \log_{10} \left[\frac{2(f/f_c)^{a_l}}{1 + (f/f_c)^{a_l - a_h}} \right]. \tag{15}$$

With Δf_{-6dB} being the bandwidth of the hump for which the pressure amplitude is equal to half the maximum amplitude, a_h being the slope of the high-frequency, and a_l being the slope of the low-frequency. The resonance frequency of the vortex f_c is derived based on theoretical considerations and the use of the experimental data of Maines and Arndt (1997), as

$$\frac{f_c}{f_{bpf}} = \tau \frac{D \sqrt{\sigma_n}}{r_c Z}, \tag{16}$$

where τ is a calibration constant, and f_{bpf} the blade passing frequency. The source level spectrum is modelled as a weighted sum of the two spectral functions H_h and H_s as

$$SL(f) = L_{p,\max} + 10 \log_{10} \left[\alpha_s 10^{H_h(f)/10} + (1 - \alpha_s) 10^{H_s(f)/10} \right], \tag{17}$$

where α_s is a calibration constant, and $L_{p,max}$ is the maximum level of the hump of the power density spectrum, given by

$$L_{p,\max} = a_p + 20 \log_{10} \left[\left(\frac{\tau r_c}{D} \right)^{k_p} \sqrt{Z} \right], \tag{18}$$
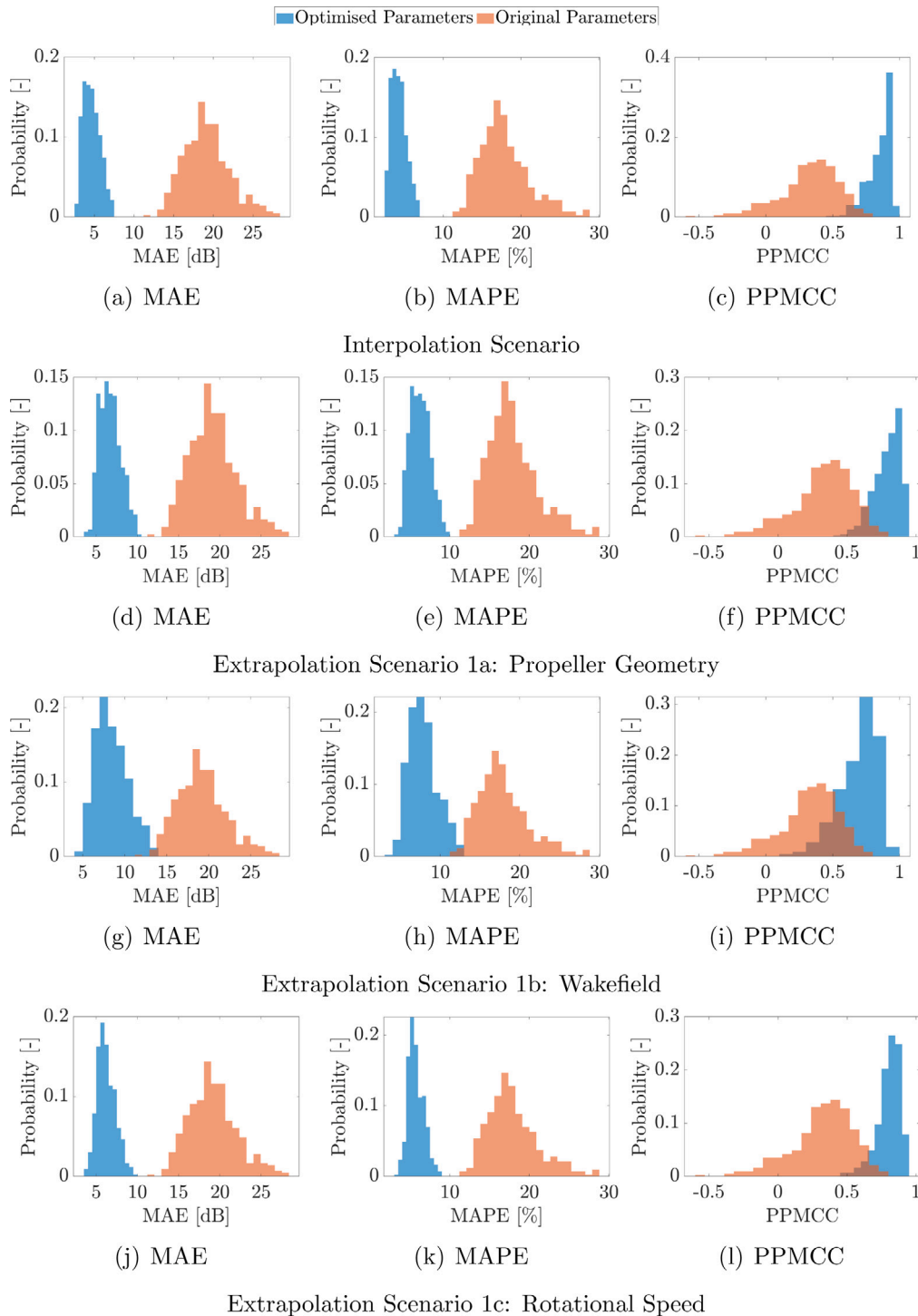
Fig. 8. Histograms of the performance metrics on the interpolation and extrapolation 1 scenarios.

with a_p and k_p being calibration constants. In Raestad (1996) $k_p = 2$ is suggested. However, we set $k_p = 3$, as it was reported to provide more accurate results in Bosschers (2018c).

4. Parameter calibration

The models of Sections 3.2–3.3 have two sets of calibration constants: a set that corresponds to the constants whose values arise from theoretical considerations, and a set that refers to constants that have to be estimated from experimental data. The constants of the latter set S are summarised in Table 3.

The Matusiak model requires the calibration of 5 constants. Note that the author in Matusiak (1992) performed a detailed calibration study and thoroughly discussed the choice of certain values along with their physical interpretation. However, the calibration process was performed using limited measurements, and certain values were chosen for reasons of computational cost that do not apply anymore.

Regarding the ETV model, 7 constants have to be calibrated, for which the author has performed an extensive analysis on several datasets, both in model-scale and full-scale data, under a variety of operating conditions (Bosschers, 2018a,c). Nevertheless, the nature of

Table 5
Physical model performance measured with the MAE, MAPE and PPMCC.

| Scenario	Calibrated parameters			Initial parameters		
	MAE	MAPE	PPMCC	MAE	MAPE	PPMCC
Interpolation	4.69 ± 0.34	4.33 ± 0.50	0.90 ± 0.06	19.35 ± 2.98	18.03 ± 3.06	0.33 ± 0.22
Extrapolation scenario 1a: Propeller geometry						
KCD 65	7.99 ± 1.10	7.70 ± 1.04	0.77 ± 0.24	18.53 ± 2.34	17.01 ± 2.33	0.41 ± 0.17
KCD 74	7.48 ± 1.02	7.10 ± 0.96	0.85 ± 0.20	19.71 ± 3.11	19.14 ± 3.41	0.28 ± 0.24
KCD 129	7.70 ± 1.04	7.28 ± 0.97	0.84 ± 0.20	19.27 ± 3.06	18.20 ± 3.52	0.32 ± 0.22
KCD 191	7.67 ± 1.02	7.14 ± 0.94	0.82 ± 0.23	19.24 ± 3.01	18.19 ± 3.58	0.34 ± 0.21
KCD 192	7.82 ± 1.04	7.31 ± 0.96	0.80 ± 0.22	18.83 ± 2.95	17.99 ± 2.36	0.31 ± 0.19
KCD 193	7.53 ± 1.02	7.00 ± 0.95	0.83 ± 0.21	19.35 ± 2.75	17.76 ± 3.19	0.30 ± 0.26
all	7.70 ± 1.03	7.20 ± 0.97	0.82 ± 0.22	19.35 ± 2.98	18.03 ± 3.06	0.33 ± 0.22
Extrapolation scenario 1b: Wakefield						
W1	8.61 ± 1.31	8.93 ± 1.41	0.77 ± 0.12	19.32 ± 2.34	18.09 ± 3.11	0.34 ± 0.27
W2	8.21 ± 1.30	8.64 ± 1.33	0.76 ± 0.11	19.24 ± 3.11	18.05 ± 3.56	0.33 ± 0.27
W3	8.44 ± 1.35	8.87 ± 1.38	0.79 ± 0.11	19.37 ± 2.96	17.49 ± 2.85	0.30 ± 0.28
all	8.41 ± 1.33	8.78 ± 1.35	0.77 ± 0.11	19.35 ± 2.98	18.03 ± 3.06	0.33 ± 0.28
Extrapolation scenario 1c: Rotational speed						
600 rpm	5.88 ± 0.77	5.30 ± 0.75	0.88 ± 0.13	18.55 ± 2.49	17.58 ± 2.42	0.43 ± 0.15
800 rpm	5.43 ± 0.65	5.52 ± 0.75	0.91 ± 0.19	19.28 ± 3.16	18.12 ± 3.29	0.27 ± 0.26
1000 rpm	6.08 ± 0.75	5.99 ± 0.80	0.82 ± 0.22	19.29 ± 2.72	18.19 ± 2.95	0.36 ± 0.17
1200 rpm	6.86 ± 0.81	6.47 ± 0.83	0.79 ± 0.18	19.45 ± 3.14	18.42 ± 3.27	0.32 ± 0.23
1400 rpm	6.59 ± 0.67	5.93 ± 0.76	0.89 ± 0.18	18.90 ± 3.03	17.74 ± 3.18	0.38 ± 0.17
1500 rpm	6.51 ± 0.90	5.81 ± 0.79	0.86 ± 0.18	19.93 ± 3.13	17.51 ± 2.62	0.26 ± 0.24
1750 rpm	6.24 ± 0.87	5.51 ± 0.74	0.85 ± 0.19	19.60 ± 2.95	18.05 ± 3.21	0.23 ± 0.23
2000 rpm	6.19 ± 0.88	5.34 ± 0.67	0.82 ± 0.21	18.89 ± 2.49	18.27 ± 2.68	0.38 ± 0.22
all	6.53 ± 0.86	5.73 ± 0.82	0.87 ± 0.18	19.35 ± 2.98	18.03 ± 3.06	0.33 ± 0.22
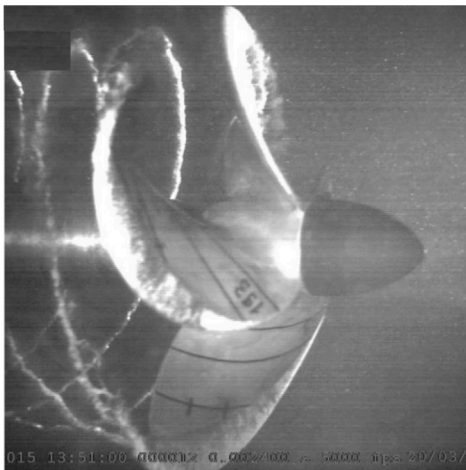
Fig. 9. Cavitation observations under atmospheric pressure for the propeller KCD 193 on W1 at 1750 [rpm] (Aktas et al., 2018).

the method requires the implementation of a calibration procedure in order to provide plausible predictions.

We could also treat certain parameters of the Gilmore equation as calibration constants, for instance, by modifying the value for the polytropic index k, which determines if the process is adiabatic ($k = 1.4$) or isothermal ($k = 1$). Moreover, the assumption that the initial gas pressure p_{g0} is equal to the vapour pressure can be refined by actually computing p_{g0}, on the basis of the initial (undisturbed) pressure outside the bubble, following the suggestion mentioned in Leighton (2012), and later implemented in Lafeber et al. (2015). Nevertheless, their values have been kept constant according to Table 2, along with the original assumption made in Matusiak (1992).

4.1. Problem formulation

The calibration process is formulated as an optimisation problem, with decision variables being the values of the calibration constants of

Table 3, and the objective (cost) function being an error metric that quantifies the difference between the actual and the predicted URN spectra. Formally, we seek the solution to the following continuous, non-convex problem

$$\arg \min_{s} \quad \hat{L}(s; \mathcal{D}_n) = \sum_{i=1}^{d} l(h(x_i, s), y_i) \tag{19}$$

subject to:　　$s_{min} \leq s \leq s_{max}.$

x denotes the model inputs, i.e. the propeller geometry, wakefield, inflow conditions, and the pressure distribution on the key blade for one complete revolution, and $y \in \mathbb{R}^p$ refers to the measured URN spectrum. $s \in S$ is the vector of the constants in Table 3 that will be calibrated from the bounded space $\{s_{min}, s_{max}\}$ of Table 4, and $\hat{L}(s, \mathcal{D}_n)$ is the empirical error of the physical model h on a dataset $\mathcal{D}_n = \{(x_1, y_1), \ldots, (x_n, y_n)\}$, measured according to a loss function l.

For the latter we adopt the square loss, given by

$$l\left(h\left(x_i, s\right), y_i\right) = \left(h(x_i, s) - y_i\right)^2. \tag{20}$$

Because y is a vector, we have re-defined the loss function as the average squared difference between the actual and predicted URN spectra. This is possible since they both represent homogeneous quantities, and the average difference between the two can describe the quality of h in a satisfactory manner.

4.2. Solution method

Given the nature of the problem, a global Derivative-Free Optimisation (DFO) method must be utilised, as obtaining or estimating the derivatives of the physical models with respect to the parameters s is a cumbersome and time-intensive procedure. The literature on DFO methods is quite large, with a variety of algorithms that can solve a diverse class of problems (Galinier et al., 2013).

We have employed Particle Swarm Optimisation (PSO) to solve problem (19) for a variety of reasons, including the reduced number of parameters that require calibration, and its computational speed in providing good quality solutions. Furthermore, its stochastic properties allow for solution variability and thorough exploration of the search space in the initial iterations, with a local search behaviour during
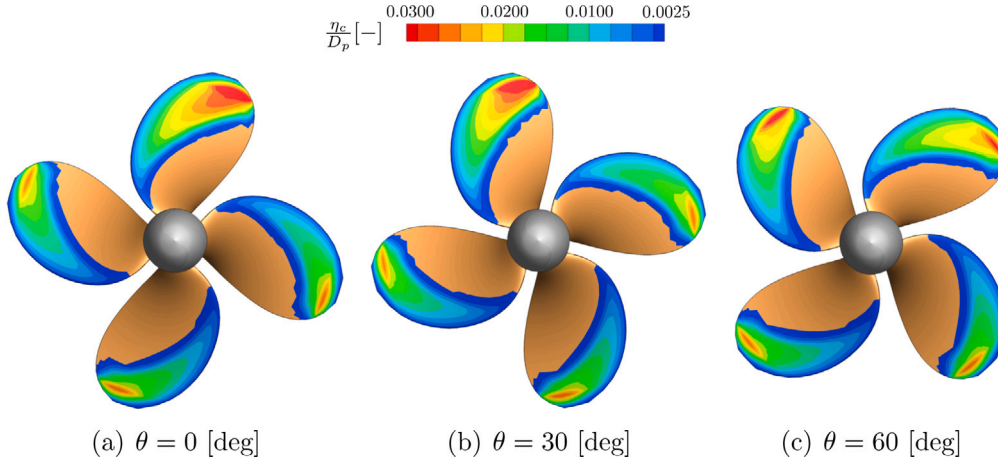
Fig. 10. Cavity thickness estimation from a fully-cavitating BEM simulation for the experiment of Fig. 9.
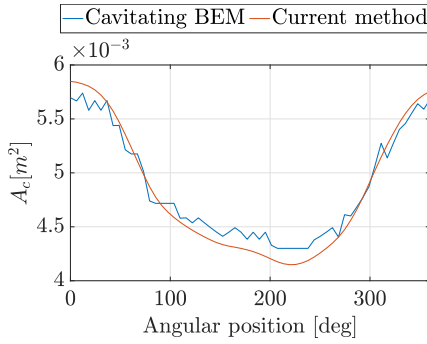

Fig. 11. Estimated cavity area on the suction side of the key blade for the experiment of Fig. 9.

the final iterations (Martinez and Cao, 2018). Finally, it is robust and well suited to handle non-linear, non-convex search spaces with discontinuities, and is readily available in most numerical platforms. Regarding the algorithm's parameters, we apply linearly decreasing inertia with a starting value of 1.15, and set the velocity of each particle to be influenced by a local neighbourhood of 90% of the entire swarm. Finally, for the velocity adjustment of each particle between iterations, the relative weighting of each particle's best position and the local neighbourhood's best position are set to 1.5.

4.3. Error estimation process

To objectively evaluate the performance of h, our experimental data $\mathcal{D}_n$ should have been split into two different subsets: The set $\mathcal{L}_l$ that is used to calibrate s by solving Problem (19), and the set $\mathcal{T}_t = \{(x_1^t, y_1^t), \ldots, (x_r^t, y_r^t)\}$ that is used to evaluate (test) the performance of h on a real-world scenario, with $\mathcal{L}_l \cap \mathcal{T}_t = \oslash$, and $\mathcal{L}_l \cup \mathcal{T}_t = \mathcal{D}_n$. $\mathcal{T}_t$ is required, since the error that h would commit over $\mathcal{L}_l$ would be too optimistically biased, as $\mathcal{L}_l$ has been used to calibrate h.

A more rigorous procedure to assess the performance of h is to utilise resampling techniques, which rely on a simple idea: Instead of splitting $\mathcal{D}_n$ to $\mathcal{L}_l$ and $\mathcal{T}_t$ just once, $\mathcal{D}_n$ is resampled one or many (n_r) times, with or without replacement, to build the independent datasets $\mathcal{L}_l^r$, and $\mathcal{T}_t^r$, with $r \in \{1, \ldots, n_r\}$, so that $\mathcal{L}_l^r \cap \mathcal{T}_t^r = \oslash$, and $\mathcal{L}_l^r \cup \mathcal{T}_t^r = \mathcal{D}_n$ for all $r \in \{1, \ldots, n_r\}$.

Subsequently, to select the best values for the calibration constants s^* we solve Problem (19) utilising only $\mathcal{L}_l^r$, and we compute an evaluation metric

$$M(h(s^*, \mathcal{L}_l^r), \mathcal{T}_t^r) \tag{21}$$

Since the data in $\mathcal{L}_l^r$ are independent from the data in $\mathcal{T}_t^r$, Eq. (21) yields an unbiased estimation of the true performance of h, measured with the metric M (Oneto, 2020).

To provide a complete description of the quality of h, we report a variety of metrics in Section 5 that refer only to its performance on $\mathcal{T}_t^r$. Assuming that $y \in \mathcal{Y}$ is scalar, we report the Mean Absolute Percentage Error (MAPE), computed as the absolute loss value of h over $\mathcal{T}_t^r$ in percentage

$$\text{MAPE}(h, \mathcal{T}_t^r) = \frac{1}{t} \sum_{i=1}^{t} \left| \frac{y_i^t - h(x_i^t)}{y_i^t} \right|, \tag{22}$$

the Mean Absolute Error (MAE), computed as the absolute loss of h over $\mathcal{T}_t^r$

$$\text{MAE}(h, \mathcal{T}_t^r) = \frac{1}{t} \sum_{i=1}^{K} \left| y_i^t - h(x_i^t) \right|, \tag{23}$$

and the Pearson Product-Moment Correlation Coefficient (PPMCC), which measures the linear dependency between $h(x_i^t)$ and y_i^t, given by

$$\text{PPMCC}(h, \mathcal{T}_t^r) = \frac{\sum_{i=1}^{t} \left(y_i^t - \bar{y} \right) \left(h(x_i^t) - \hat{y} \right)}{\sqrt{\sum_{i=1}^{t} \left(y_i^t - \bar{y} \right)^2} \sqrt{\sum_{i=1}^{t} \left(h(x_i^t) - \hat{y} \right)^2}}, \tag{24}$$

where $\bar{y} = \frac{1}{t} \sum_{i=1}^{t} y_i^t$ and $\hat{y} = \frac{1}{t} \sum_{i=1}^{t} h(x_i)$. Other state-of-the-art error measures exist, but from a physical point of view, the ones already reported give a complete description of the quality of h (Miglianti et al., 2019, 2020).

However, $\mathcal{Y} \subseteq \mathbb{R}^p$ is a vector representing the URN spectra instead of a scalar quantity. Similar to the loss function of Eq. (20), we redefine the error metrics of Eqs. (22)–(24) as the average metrics of the quantities that compose the URN spectra. Namely, these metrics quantify the difference between the measured and predicted URN spectrum at a reference pressure of 1 MPa, corrected at a measuring distance of 1m, at different frequencies in the 1/3 octave band.

5. Results and discussion

5.1. Experimental setting

In this section the performance of the models is tested utilising the data described in Section 2 and the performance measures defined in Section 4.3, in three scenarios. These scenarios differ only in the way the dataset $\mathcal{D}_n$ is split on $\mathcal{L}_l^r$ and $\mathcal{T}_t^r$ at each repetition, and they consist of:

• Interpolation Scenario: In this case the computational models aim to predict the URN spectra in various experiments that lie within the ones utilised to calibrate them. $\mathcal{D}_n$ is split randomly $n_r = 10$ times, keeping 90% of the experiments in $\mathcal{L}_l^r$, and the remaining 10% in $\mathcal{T}_t^r$.
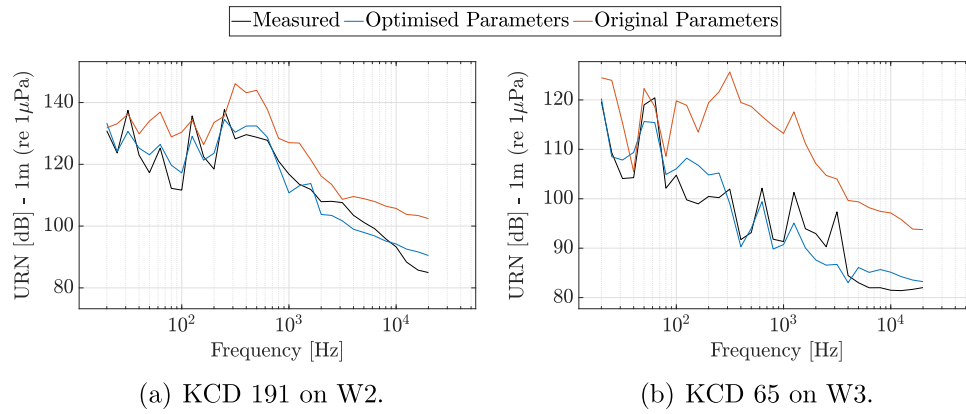
(a) KCD 191 on W2.

(b) KCD 65 on W3.

Fig. 12. Computational and experimental results on two example cases from the interpolation scenario.
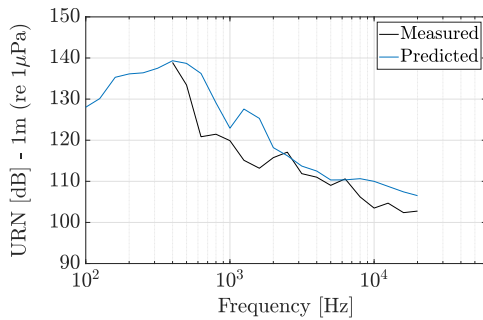

Fig. 13. Computational results on extrapolation scenario 2.

- Extrapolation Scenario 1: In this case the models aim to predict the URN spectra in groups of experiments that lie outside the ones utilised to calibrate them. In this context, we have performed the following scenarios:

  - Scenario 1a: Extrapolation on the propeller geometry, in which $\mathcal{T}_t^r$ consists of the group of experiments conducted on one specific propeller from the Meridian standard series. Given that $\mathcal{D}_n$ consists of 6 propeller geometries, this scenario has been repeated $n_r = 6$ times, each with experiments of a different propeller in $\mathcal{T}_t^r$.
  - Scenario 1b: Extrapolation on the wakefield, where $\mathcal{T}_t^r$ contains all experiments involving a specific wakefield, for a total of $n_r = 3$ repetitions.
  - Scenario 1c: Extrapolation on the rotational speed of the propeller, with $\mathcal{T}_t^r$ containing all experiments conducted with a specific rotational speed, with a total of $n_r = 8$ repetitions.

- Extrapolation Scenario 2: In this case the models aim to predict the URN spectra of the propeller of Fig. 6 in uniform wakefield.

By conducting the interpolation scenario, we test the ability of the models to predict the URN spectra in various, slightly different, operating conditions than the ones utilised to calibrate the constants s. The extrapolation scenarios allow us to test the capabilities of the models to predict the URN spectra for cases not included in the experiments used to calibrate s, which generally correspond to more realistic scenarios encountered in practice. By conducting the extrapolation scenario 1 we can thus quantify the expected errors when predicting URN on a new propeller geometry, a different wakefield, or different operating conditions. Extrapolation Scenario 2, although limited as it consists of a single case, it allows us to get a first impression on model performance when the entire input domain is different from $\mathcal{D}_n$, with propeller geometry, wakefield, and inflow conditions varying simultaneously.

For each of these tests we have conducted the calibration process described in Section 4 utilising the corresponding $\mathcal{L}_l^r$, and we report average results together with their t-student 95% confidence interval for each $\mathcal{T}_t^r$, to ensure statistical consistency. The only exception is extrapolation scenario 2, which does not involve resampling. Strictly for this scenario, $\mathcal{D}_n$ in its entirety has been utilised to calibrate the parameters, and $\mathcal{T}$ consists solely of the propeller of Fig. 6 in uniform wakefield. For the sake of comparison, we also report results for the interpolation scenario and extrapolation scenario 1 when utilising the initial parameter values reported in Matusiak (1992), Bosschers (2018a) and presented in Table 3.

5.2. Assessment of noise predictions

Table 5 reports the various error metrics on the Interpolation and Extrapolation 1 scenarios, for both the calibrated and initial values of the model's parameters. It is possible to observe that the performance of the models is significantly better with the calibrated parameters, with error reductions of approximately 75% in the interpolation scenario, 66% when extrapolating on the propeller geometry and rotational speed, and 50% on wakefield extrapolation. Using the values reported in Matusiak (1992) and Bosschers (2018a) we observe average errors of approximately 18%, or 19 dB for all scenarios, with weak linear associations between measured and predicted URN, as revealed by the relatively low values of PPMCC. The calibration process reduces these errors to approximately 4.3%, or 4.7 dB in the interpolation scenario, 7.2% or 7.7 dB when extrapolating on the propeller geometry, 5.7% or 6.5 dB when extrapolating on the rotational speed, and 8.8% or 8.4 dB for wakefield extrapolation, all with considerable drop in the variance as well, as the error distributions of Fig. 8 show.

For what regards the performance of the calibrated models, it is possible to observe that the experimental data can be modelled effectively on all scenarios. As expected, lowest errors are observed for the interpolation scenario. Extrapolation errors are increased by 50% to 100% depending on the scenario. Among those, lowest errors are observed when extrapolating on the rotational speed of the propeller (scenario 1c), for which the errors appear to be consistent for all rotational speeds, and vary between $(5.4 \pm 0.65, 5.5 \pm 0.75, 0.91 \pm 0.19)$ [dB, %, –] at 800 rpm, to $(6.9 \pm 0.8, 6.5 \pm 0.8, 0.79 \pm 0.18)$ [dB, %, –] at 1200 rpm for MAE, MAPE, and PPMCC, respectively. This occurs due to the relatively small changes in the cavitation patterns observed with small variations in the rotational speed, so $\mathcal{L}_l^r$ and $\mathcal{T}_t^r$ have relatively small differences with respect to the URN spectra. A more difficult case is the extrapolation on the propeller geometry (scenario 1a). In this case, errors between $(7.5 \pm 1.0, 7.1 \pm 1.0, 0.85 \pm 0.20)$ [dB, %, –] and $(8.0 \pm 1.1, 7.7 \pm 1.0, 0.77 \pm 0.24)$ are observed, which correspond to propellers KCD 74 and KCD 65, respectively. Overall, small error variations exist among all the different propeller geometries, underlining the stability

of the approaches. Highest discrepancies are observed for the wakefield extrapolation (scenario 1b), with errors being fairly consistent among all 3 wakefields to about $(8.4 \pm 1.3, 8.8 \pm 1.35, 0.77 \pm 0.11)$ [dB, %, –], approximately double with respect to the interpolation scenario. The difficulty of this scenario occurs due to the high differences in the cavitation patterns occurring with each wakefield, resulting in more "severe" extrapolation cases. Note that the wakefields employed in this work were chosen specifically for this reason, as discussed in Aktas (2017) and Aktas et al. (2018). Nevertheless, the performance of the models is widely acceptable even for this scenario, with a maximum difference of only 8.6 ± 1.3 dB, or $8.9 \pm 1.4\%$ for $W1$.

5.3. Additional results on representative cases

For the sake of brevity we do not report individual results on every experiment and scenario due to the size of the dataset and the number of experiments we performed. Nevertheless, it is worth exploring the results of some representative cases to gain a better understanding regarding the prediction capabilities of the proposed models. Fig. 9 illustrates the cavitation observed during the experiment conducted for the propeller KCD 193 on W1 at 1750 [rpm] under atmospheric pressure conditions. Unfortunately, the available experimental data related to cavitation patterns do not allow us to perform thorough quantitative comparisons between experimental and computational results. For this reason we have performed a fully cavitating BEM simulation for the experiment of Fig. 9, which can provide us with a reasonable estimation of the cavity extent on the propeller blades. Subsequently, we can compare this estimation with the cavity extent predicted with the models of Section 3.

Fig. 9 provides the predicted cavity thickness obtained with the fully cavitating BEM for three angular positions. A visual comparison between Figs. 9 and 10(a) shows that the cavity extent can be predicted with satisfactory accuracy. From the estimated cavity thickness we have evaluated the total cavity area on the suction side of the key-blade over one complete propeller revolution. The same quantity has also been extracted from the models of Section 3, and is compared with the fully cavitating BEM estimations on Fig. 11. As can be seen, the estimated cavity area is adequately captured by the models proposed in this work: the resulting trends are physically plausible and agree reasonably well with the results of the fully cavitating BEM. However, differences are observed for angular locations between 90–270 [deg], characterised by smaller cavities, for which the cavity area is consistently underestimated. Nevertheless, the maximum difference that occurs at approximately 215 [deg] remains below 5.4[%], which can be considered acceptable for early stage design studies.

A graphical illustration of representative URN spectra during the interpolation scenario is provided in Fig. 12. For both the initial and calibrated model parameters, Fig. 12(a) corresponds to the experiment predicted with the highest accuracy (KCD191 with the wakefield W2), and Fig. 12(b) to the experiment with the highest discrepancy between measurements and predictions (KCD65 with the wakefield W3). It is interesting to note that the calibrated parameter set does not significantly affect the predictions on Fig. 12(a). However, significant differences exist for the experiment of Fig. 12(b), for which the calibrated models do not overestimate the URN levels, and show a more plausible trend.

An overall error reduction is expected when calibrating the parameters of these models, for the reasons underlined in Sections 3.2–3.3. Nevertheless, the results indicate that there are notable, statistically significant differences, regardless of the scenario considered. To the extent that the available data allow us to draw conclusions, it appears that a proper calibration process can render these semi-empirical models powerful enough for the early design process. The same conclusion can be drawn from Fig. 13, which presents the predicted and measured URN spectra for extrapolation scenario 2. The models are able to predict URN with acceptable accuracy, with the average error between measurements and predictions being approximately 9 [dB], and a maximum difference of 16 [dB] occurring at 600 [Hz].

Table 6
Optimised parameters of the semi-empirical models.

Method	Symbol	Equation	Value	Symbol	Equation	Value
Matusiak model (Section 3.2)	β_f	Eq. (3)	0.6	m	Eq. (4)	5
	n_b	Eq. (3)	500	c_b	Eq. (4)	3.8
	τ_b	Eq. (10)	350			
ETV model (Section 3.3)	ζ_3	Eq. (13)	11.6	Δf_{-6dB}	Eq. (14)	13.8
	a_l	Eq. (15)	3.85	a_h	Eq. (15)	−1.86
	τ	Eq. (16)	0.92	α_s	Eq. (17)	0.65
	a_p	Eq. (18)	118			

5.4. Calibrated parameter values

Note that, whereas for every scenario and resampling we obtain slightly different parameter values as each $\mathcal{L}_l^r$ varies, the values that will be utilised in practice are obtained when the models have been parameterised on $\mathcal{D}_n$ in its entirety (extrapolation scenario 2). These values are presented in Table 6. It is worth noting that the values of the calibration constants for the ETV model showed deviations no more than $\pm 10\%$ compared to the values proposed in Bosschers (2018a), in line with their physical interpretation. However, we observed significant differences for the parameters of the Matusiak model, which are worthy of attention due to their inherent physical meaning. More specifically, the parameter τ_b, which controls the number of oscillations for which the bubble motion is simulated, has an optimal value of 350. Physically, this implies that bubble motion was simulated as long as possible, until the oscillations have been essentially dampened out. Furthermore, the fractal order m of the size distribution of the bubbles also reduced from its initial value of 9, to 5 for most of the scenarios studied, the gas/vapour fraction β_f was also reduced to 0.6, and the constant c_b that controls the cavity thickness at the point of break-off was increased to a value of 3.8 from the recommended value of 1.8 in Matusiak (1992), signifying the presence of larger bubbles. Finally, the number of bubble classes n_b also increased dramatically from the initial value of 5 to 500 for most of the experiments, which corresponds to the upper limit set during the calibration process. This essentially implies the requirement that each bubble be treated individually, or the use of a very fine discretisation grid to obtain accurate results, as also reported in Lafeber et al. (2015).

6. Conclusions

In this work we investigated the potential of computationally cheap semi-empirical models to accurately estimate propeller cavitation noise, with information that is usually available during the early design process. To evaluate the prediction capabilities of these models, an extensive dataset has been utilised, collected through model scale tests in a cavitation tunnel. An in-depth investigation of the performance of the models has been performed. The comparison between the predicted noise levels and the experimental results has shown sufficiently good agreement. This indicates that, when properly calibrated, the combination of the ETV model, responsible for predicting noise due to a cavitating tip vortex, and the model of Matusiak, responsible for predicting the broadband effects of sheet cavitation, can be a convenient solution for the practical evaluation of propeller cavitation noise.

In particular, three sets of evaluations have been carried out. In the first set, the capability of the models to predict the main characteristics of the URN spectra in operating conditions within the ones utilised to calibrate them has been analysed; in all cases, the investigations have been conducted with conditions different from those used for the calibration process, but always remaining inside the initial input domain. In the second set of evaluations, we tested the capability of the models to predict the URN spectra in groups of operating conditions where the cavitation pattern is different with respect to the one employed to calibrate them. In the final evaluation, we assessed the

performance of the models to predict the URN spectra on 1 additional propeller, completely unrelated to the available experimental data. In all scenarios the models have shown accurate results. The errors reported during extrapolation increased between 50% to 100%, compared to interpolation. Nevertheless, all errors still lie below 9 dB, and can be considered satisfactory in practical applications.

The present analysis has been limited to a certain set of propellers and wakefields deemed of interest due to their commercial consideration, and ability to generate a dataset of tolerable variance. For this reason, further activities include additional data collection to compile a richer set of propellers and wakefields, and the combination of physical models with data-driven approaches, to further enhance overall prediction performance while keeping the computational effort as low as possible.

CRediT authorship contribution statement

Miltiadis Kalikatzarakis: Conceptualisation, Methodology, Data curation, Software, Validation, Writing – original draft, Writing – review & editing. **Andrea Coraddu:** Conceptualisation, Methodology, Data curation, Writing – original draft, Writing – review & editing. **Mehmet Atlar:** Data source, Writing – review & editing. **Stefano Gaggero:** Conceptualisation, Methodology, Data curation, Writing – original draft, Writing – review & editing. **Giorgio Tani:** Conceptualisation, Methodology, Data curation, Writing – original draft, Writing – review & editing. **Diego Villa:** Conceptualisation, Methodology, Writing – review & editing. **Luca Oneto:** Conceptualisation, Methodology, Writing – original draft, Writing – review & editing.

Declaration of competing interest

The authors declare that they have no known competing financial interests or personal relationships that could have appeared to influence the work reported in this paper.

Acknowledgements

References

Aktas, B., 2017. A Systematic Experimental Approach to Cavitation Noise Prediction of Marine Propellers (Ph.D. thesis). Newcastle University.

Aktas, B., Atlar, M., Fitzsimmons, P., Shi, W., 2018. An advanced joint time-frequency analysis procedure to study cavitation-induced noise by using standard series propeller data. Ocean Eng. 170, 329–350.

Aktas, B., Atlar, M., Turkmen, S., Shi, W., Sampson, R., Korkut, E., Fitzsimmons, P., 2016. Propeller cavitation noise investigations of a research vessel using medium size cavitation tunnel tests and full-scale trials. Ocean Eng. 120, 122–135.

Andersen, P., Friesch, J., Kappel, J.J., Lundegaard, L., Patience, G., 2005. Development of a marine propeller with nonplanar lifting surfaces. Mar. Technol. 42 (03), 144–158.

Andersen, P., Kappel, J.J., Spangenberg, E., 2009. Aspects of propeller developments for a submarine. In: First International Symposium on Marine Propulsors, Trondheim, Norway. pp. 723–736.

Ando, T., Kimura, K., Suyama, N., Yamamoto, K., 1976. Study on cavitation and noise performance of marine propellers using CFD analysis. In: 18th Symposium on Cavitation.

Angelopoulos, A., Fitzsimmons, P.A., Odabasi, A.Y., 1988. A Semi-Empirical Method for Propeller Broad-Band Noise. Technical report, British Maritime Technology Limited.

Asnaghi, A., Svennberg, U., Bensow, R.E., 2018. Numerical and experimental analysis of cavitation inception behaviour for high-skewed low-noise propellers. Appl. Ocean Res. 79, 197–214.

Asnaghi, A., Svennberg, U., Bensow, R.E., 2020. Large eddy simulations of cavitating tip vortex flows. Ocean Eng. 195, 106703.

Atlar, M., 2011. Recent upgrading of marine testing facilities at newcastle university. In: Second International Conference on Advanced Model Measurement Technology for the EU Maritime Industry. pp. 4–6.

Bensow, R., Liefvendahl, M., 2016. An acoustic analogy and scale-resolving flow simulation methodology for the prediction of propeller radiated noise. In: 31st Symposium on Naval Hydrodynamics. pp. 11–16.

Bertetta, D., Brizzolara, S., Gaggero, S., Viviani, M., Savio, L., 2012. CPP propeller cavitation and noise optimization at different pitches with panel code and validation by cavitation tunnel measurements. Ocean Eng. 53, 177–195.

Borelli, D., Gaggero, T., Rizzuto, R., Schenone, C., 2021. Onboard ship noise: Acoustic comfort in cabins. Appl. Acoust. 177, 107912.

Bosschers, J., 2009. Investigation of hull pressure fluctuations generated by cavitating vortices. In: First Symposium on Marine Propulsors.

Bosschers, J., 2017. A semi-empirical method to predict broadband hull pressure fluctuations and underwater radiated noise by cavitating tip vortices. In: Fifth International Symposium on Marine Propulsors.

Bosschers, J., 2018a. Propeller Tip-Vortex Cavitation and its Broadband Noise (Ph.D. thesis). University of Twente.

Bosschers, J., 2018b. An analytical and semi-empirical model for the viscous flow around a vortex cavity. Int. J. Multiph. Flow. 105, 122–133.

Bosschers, J., 2018c. A semi-empirical prediction method for broadband hull-pressure fluctuations and underwater radiated noise by propeller tip vortex cavitation. J. Mar. Sci. Eng. 6 (2), 49.

Bosschers, J., Choi, G.H., Hyundai, H.I., Farabee, K.T., Fréchou, D., Korkut, E., Sato, K., et al., 2017. Specialist committee on hydrodynamic noise. In: Final Report and Recommendations to the 28th International Towing Tank Conference. Specialist Committee on Hydrodynamic Noise, Vol. 45.

Brennen, C.E., 2014. Cavitation and Bubble Dynamics. Cambridge University Press.

Brentner, K.S., Farassat, F., 2003. Modeling aerodynamically generated sound of helicopter rotors. Prog. Aerosp. Sci. 39 (2–3), 83–120.

Brooker, A., Humphrey, V., 2016. Measurement of radiated underwater noise from a small research vessel in shallow water. Ocean Eng. 120, 182–189.

Brown, N.A., 1976. Cavitation noise problems and solutions. In: International Symposium on Shipboard Acoustics.

Brown, N.A., 1999. Thruster noise. In: Dynamic Positioning Conference.

Capone, A., Di Felice, F., Pereira, F.A., 2021. On the flow field induced by two counter-rotating propellers at varying load conditions. Ocean Eng. 221, 108322.

Carlton, J., 2018. Marine Propellers and Propulsion. Butterworth-Heinemann.

Chou, E., Southall, B.L., Robards, M., Rosenbaum, H.C., 2021. International policy, recommendations, actions and mitigation efforts of anthropogenic underwater noise. Ocean Coast. Manage. 202, 105427.

Convention on Biological Diversity, 2014. Report of the Expert Workshop on Underwater Noise and its Impacts on Marine and Coastal Biodiversity.

Da-Qing, L., 2006. Validation of RANS predictions of open water performance of a highly skewed propeller with experiments. J. Hydrodyn. Ser. B 18 (3), 520–528.

Di Franco, E., Pierson, P., Di Iorio, L., Calò, A., Cottalorda, J.M., Derijard, B., Di Franco, A., Galvé, A., Guibbolini, M., Lebrun, J., et al., 2020. Effects of marine noise pollution on Mediterranean fishes and invertebrates: A review. Mar. Pollut. Bull. 159, 111450.

Ebrahimi, A., Razaghian, A.H., Seif, M.S., Zahedi, F., Nouri-Borujerdi, A., 2019. A comprehensive study on noise reduction methods of marine propellers and design procedures. Appl. Acoust. 150, 55–69.

Ekinci, S., Celik, F., Guner, M., 2010. A practical noise prediction method for cavitating marine propellers. Shipbuild.: Theory Pract. Shipbuild. Mar. Eng. 61 (4), 359–366.

Emerson, A., 1978. Propeller design and model experiments.. Trans. North-East Coast Inst. Eng. Shipbuild. 944, 199–234.

Erbe, C., Marley, S.A., Schoeman, R.P., Smith, J.N., Trigg, L.E., Embling, C.B., 2019. The effects of ship noise on marine mammals—a review. Front. Mar. Sci. 6, 606.

Erbe, C., Reichmuth, C., Cunningham, K., Lucke, K., Dooling, R., 2016. Communication masking in marine mammals: A review and research strategy. Mar. Pollut. Bull. 103 (1–2), 15–38.

European Union, 2008. Establishing a Framework for Community Action in the Field of Marine Environmental Policy (Marine Strategy Framework Directive). Official Journal of the European Union.

European Union, 2017a. Laying Down Criteria and Methodological Standards on Good Environmental Status of Marine Waters and Specifications and Standardized Methods for Monitoring and Assessment. Official Journal of the European Union.

European Union, 2017b. United Nations Open-Ended Informal Consulative Process on Oceans and the Law of the Sea - the Effects of Anthropogenic Underwater Noise, Contribution of the European Union. Official Journal of the European Union.

Farassat, F., Brentner, K.S., 1988. The uses and abuses of the acoustic analogy in helicopter rotor noise prediction. J. Am. Helicopter Soc. 33 (1), 29–36.

Ferrier-Pagès, C., Leal, M.C., Calado, R., Schmid, D.W., Bertucci, F., Lecchini, D., Allemand, D., 2021. Noise pollution on coral reefs?—A yet underestimated threat to coral reef communities. Mar. Pollut. Bull. 165, 112129.

Ffowcs Williams, J.E., 1969. Sound generated by turbulence and surfaces in arbitrary motion. Philos. Trans. R. Soc. A264.

Franc, J.P., Michel, J.M., 2006. Fundamentals of Cavitation, Vol. 76. Springer science & Business media.

Gaggero, S., Brizzolara, S., 2009. A panel method for trans-cavitating marine propellers. In: 7th International Symposium on Cavitation.

Gaggero, S., Dubbioso, G., Villa, D., Muscari, R., Viviani, M., 2019. Propeller modeling approaches for off–design operative conditions. Ocean Eng. 178, 283–305.

Gaggero, S., Gonzalez-Adalid, J., Sobrino, M.P., 2016a. Design and analysis of a new generation of CLT propellers. Appl. Ocean Res. 59, 424–450.

Gaggero, S., Gonzalez-Adalid, J., Sobrino, M.P., 2016b. Design of contracted and tip loaded propellers by using boundary element methods and optimization algorithms. Appl. Ocean Res. 55, 102–129.

Gaggero, S., Tani, G., Villa, D., Viviani, M., Ausonio, P., Travi, P., Bizzarri, G., Serra, F., 2017a. Efficient and multi-objective cavitating propeller optimization: An application to a high-speed craft. Appl. Ocean Res. 64, 31–57.

Gaggero, S., Villa, D., 2017. Steady cavitating propeller performance by using Open-FOAM, StarCCM+ and a boundary element method. Proc. Inst. Mech. Eng. M 231 (2), 411–440.

Gaggero, S., Villa, D., 2018. Cavitating propeller performance in inclined shaft conditions with OpenFOAM: PPTC 2015 test case. J. Mar. Sci. Appl. 17 (1), 1–20.

Gaggero, S., Villa, D., Brizzolara, S., 2010. RANS and PANEL method for unsteady flow propeller analysis. J. Hydrodyn. Ser. B 22 (5), 564–569.

Gaggero, S., Villa, D., Tani, G., Viviani, M., Bertetta, D., 2017b. Design of ducted propeller nozzles through a RANSE-based optimization approach. Ocean Eng. 145, 444–463.

Gaggero, S., Villa, D., Viviani, M., 2014. An investigation on the discrepancies between RANSE and BEM approaches for the prediction of marine propeller unsteady performances in strongly non-homogeneous wakes. In: International Conference on Offshore Mechanics and Arctic Engineering.

Gaggero, S., Viviani, M., Tani, G., Conti, F., Becchi, P., Valdenazzi, F., 2013. Comparison of different approaches for the design and analysis of ducted propellers. In: 5th International Conference on Computational Methods in Marine Engineering. pp. 723–736.

Galinier, P., Hamiez, J.P., Hao, J.K., Porumbel, D., 2013. Handbook of Optimization. Springer.

Ge, M., Svennberg, U., Bensow, R.E., 2020. Investigation on RANS prediction of propeller induced pressure pulses and sheet-tip cavitation interactions in behind hull condition. Ocean Eng. 209, 107503.

Geurst, J.A., 1961. Linearized Theory of Two-Dimensional Cavity Flows (Ph.D. thesis). Delft University of Technology.

Gilmore, F.R., 1952. The Growth or Collapse of a Spherical Bubble in a Viscous Compressible Liquid. Technical report, California Institute of Technology.

Hildebrand, J.A., 2005. Impacts of anthropogenic sound. In: Marine Mammal Research: Conservation beyond Crisis. pp. 101–124.

Hildebrand, J.A., 2009. Anthropogenic and natural sources of ambient noise in the ocean. Mar. Ecol. Prog. Ser. 395, 5–20.

Hommes, T., Bosschers, J., Hoeijmakers, H., 2015. Evaluation of the radial pressure distribution of vortex models and comparison with experimental data. In: Journal of Physics: Conference Series, Vol. 656. pp. 171–182.

Hsin, C., 1990. Development and Analysis of Panel Methods for Propellers in Unsteady Flow (Ph.D. thesis). Massachusetts Institute of Technology.

Hu, J., Wang, Y., Zhang, W., Chang, X., Zhao, W., 2019. Tip vortex prediction for contra-rotating propeller using large eddy simulation. Ocean Eng. 194, 106410.

Hu, J., Zhang, W., Wang, C., Sun, S., Guo, C., 2021. Impact of skew on propeller tip vortex cavitation. Ocean Eng. 220, 108479.

Huang, Y.S., Dong, X.Q., Yang, C.J., Li, W., Noblesse, F., 2019a. Design of wake-adapted contra-rotating propellers for high-speed underwater vehicles. Appl. Ocean Res. 91, 101880.

Huang, Y.S., Yang, J., Yang, C.J., 2019b. Numerical prediction of the effective wake profiles of a high-speed underwater vehicle with contra-rotating propellers. Appl. Ocean Res. 84, 242–249.

Ianniello, S., De Bernardis, E., 2015. Farassat's formulations in marine propeller hydroacoustics. Int. J. Aeroacoust. 14 (1–2), 87–103.

Ianniello, S., Muscari, R., Di Mascio, A., 2013. Ship underwater noise assessment by the acoustic analogy. Part I: nonlinear analysis of a marine propeller in a uniform flow. J. Mar. Sci. Technol. 18 (4), 547–570.

Ianniello, S., Muscari, R., Di Mascio, A., 2014a. Ship underwater noise assessment by the Acoustic Analogy part II: hydroacoustic analysis of a ship scaled model. J. Mar. Sci. Technol. 19 (1), 52–74.

Ianniello, S., Muscari, R., Di Mascio, A., 2014b. Ship underwater noise assessment by the acoustic analogy, part III: measurements versus numerical predictions on a full-scale ship. J. Mar. Sci. Technol. 19 (2), 125–142.

IMO, 2012. Resolution MSC.337(91) (XII) - Code on Noise Levels on Board Ships. International Maritime Organization.

IMO, 2014. Guidelines for the Reduction of Underwater Noise from Commercial Shipping to Address Adverse Impacts on Marine Life. International Maritime Organization.

ITTC Specialist Committee on Hydrodynamic Noise, 2017. Model scale cavitation test. In: Recommended Procedures and Guidelines 7.5-01-02-05 International Towing Tank Conference.

Jessup, S.D., 1989. An Experimental Investigation of Viscous Aspects of Propeller Blade Flow (Ph.D. thesis). The Catholic University of America.

Kamiirisa, H., Goto, H., 2005. Development of prediction method for ship underwater noise by bubble dynamics. Mitsui Zosen Tech. Rev. 2 (185), 38–44.

Kanemaru, T., Ando, J., 2015. Numerical analysis of tip cavitation on marine propeller with wake alignment using a simple surface panel method "SQCM". In: Journal of Physics: Conference Series, Vol. 656. 012184.

Kellett, P., Turan, O., Incecik, A., 2013. A study of numerical ship underwater noise prediction. Ocean Eng. 66, 113–120.

Kim, S., Kinnas, S.A., 2021. Prediction of cavitating performance of a tip loaded propeller and its induced hull pressures. Ocean Eng. 229, 108961.

Konno, A., Wakabayashi, K., Yamaguchi, H., Maeda, M., Ishii, N., Soejima, S., Kimura, K., 2002. On the mechanism of the bursting phenomena of propeller tip vortex cavitation. J. Mar. Sci. Technol. 6 (4), 181–192.

Ku, G., Cho, J., Cheong, C., Seol, H., 2021. Numerical investigation of tip-vortex cavitation noise of submarine propellers using hybrid computational hydro-acoustic approach. Ocean Eng. 238, 109693.

Lafeber, F.H., Bosschers, J., 2016. Validation of computational and experimental prediction methods for the underwater radiated noise of a small research vessel. In: Proceedings of PRADS.

Lafeber, F.H., Bosschers, J., van Wijngaarden, E., 2015. Computational and experimental prediction of propeller cavitation noise. In: OCEANS 2015. pp. 1–9.

Lee, Y.H., Yang, C.Y., Chow, Y.C., 2021. Evaluations of the outcome variability of RANS simulations for marine propellers due to tunable parameters of cavitation models. Ocean Eng. 226, 108805.

Leighton, T., 2012. The Acoustic Bubble. Academic Press.

Li, D., Hallander, J., Johansson, T., 2018. Predicting underwater radiated noise of a full scale ship with model testing and numerical methods. Ocean Eng. 161, 121–135.

Lidtke, A.K., 2017. Predicting Radiated Noise of Marine Propellers using Acoustic Analogies and Hybrid Eulerian-Lagrangian Cavitation Models (Ph.D. thesis). University of Southampton.

Lidtke, A.K., Lloyd, T., Vaz, G., 2019. Acoustic modelling of a propeller subject to non-uniform inflow. In: 6th International Symposium on Marine Propulsors, SMP2019, Rome, Italy.

2021. LIFE-PIAQUO: Underwater noise impact reduction of the maritime traffic and real-time adaptation to ecosystems. http://lifepiaquo-urn.eu/en/home/. Accessed: 2021-11-01.

Lloyd, T.P., Lidtke, A.K., Rijpkemac, D.R., et al., 2015a. Using the FW-H equation for hydroacoustics of propellers. In: Proceedings of the Numerical Towing Tank Symposium (NuTTS). pp. 28–30.

Lloyd, T.P., Rijpkema, D., Van Wijngaarden, E., 2014. Implementing the ffowcs williams-hawkings acoustic analogy into a viscous CFD solver. In: 17th Numerical Towing Tank Symposium (NuTTS).

Lloyd, T., Rijpkema, D., van Wijngaarden, E., 2015b. Marine propeller acoustic modelling: comparing CFD results with an acoustic analogy method. In: 4th International Symposium on Marine Propulsors.

Long, Y., Han, C., Ji, B., Long, X., Wang, Y., 2020. Verification and validation of large eddy simulations of cavitating flow around two marine propellers with emphasis on the skew angle effects. Appl. Ocean Res. 101, 102167.

Long, Y., Han, C., Long, X., Ji, B., Huang, H., 2021. Verification and validation of Delayed Detached Eddy Simulation for cavitating turbulent flow around a hydrofoil and a marine propeller behind the hull. Appl. Math. Model. 96, 382–401.

Long, Y., Long, X., Ji, B., Xing, T., 2019. Verification and validation of Large Eddy Simulation of attached cavitating flow around a Clark-Y hydrofoil. Int. J. Multiph. Flow. 115, 93–107.

Lurton, X., 2002. An Introduction to Underwater Acoustics: Principles and Applications. Springer Science & Business Media.

Maines, B., Arndt, R., 1997. The case of the singing vortex. J. Fluids Eng. 119, 271–276.

Markus, T., Sánchez, P., 2018. Managing and regulating underwater noise pollution. In: Handbook on Marine Environment Protection. Springer, pp. 971–995.

Martinez, C.M., Cao, D., 2018. iHorizon-Enabled Energy Management for Electrified Vehicles. Butterworth-Heinemann.

Matusiak, J., 1992. Pressure and Noise Induced by a Cavitating Marine Screw Propeller (Ph.D. thesis). Aalto University.

McKenna, M.F., Gabriele, C., Kipple, B., 2017. Effects of marine vessel management on the underwater acoustic environment of Glacier Bay National Park, AK. Ocean Coast. Manage. 139, 102–112.

Melissaris, T., Schenke, S., Bulten, N., van Terwisga, T., 2020. On the accuracy of predicting cavitation impact loads on marine propellers. Wear 456, 203393.

Miglianti, L., Cipollini, F., Oneto, L., Tani, G., Gaggero, S., Coraddu, A., Viviani, M., 2020. Predicting the cavitating marine propeller noise at design stage: A deep learning based approach. Ocean Eng. 209, 107481.

Miglianti, F., Cipollini, F., Oneto, L., Tani, G., Viviani, M., 2019. Model scale cavitation noise spectra prediction: Combining physical knowledge with data science. Ocean Eng. 178, 185–203.

Morino, L., Kuo, C., 1974. Subsonic potential aerodynamics for complex configurations: a general theory. AIAA J. 12 (2), 191–197.

Nouri, N.M., Mohammadi, S., Zarezadeh, M., 2018. Optimization of a marine contra-rotating propellers set. Ocean Eng. 167, 397–404.

Odabasi, A., Fitzsimmons, P.A., 1978. Alternative methods for wake quality assessment. Int. Shipbuild. Prog. 25 (282), 34–42.

Okamura, N., Asano, T., 1988. Prediction of propeller cavitation noise and its comparison with full scale measurement. J. Soc. Nav. Archit. Japan 1988 (164), 43–53.

Oneto, L., 2020. Model Selection and Error Estimation in a Nutshell. Springer.

Peters, A., Lantermann, U., el Moctar, O., 2018. Numerical prediction of cavitation erosion on a ship propeller in model-and full-scale. Wear 408, 1–12.

Popper, A.N., Hawkins, A., 2016. The Effects of Noise on Aquatic Life II. Springer.

Proctor, F., Ahmad, N., Switzer, G., Limon Duparcmeur, F., 2010. Three-phased wake vortex decay. In: AIAA Atmospheric and Space Environments Conference.

Raestad, A.E., 1996. Tip vortex index-an engineering approach to propeller noise prediction. Nav. Archit..

Ross, D., 1976. Mechanics of Underwater Noise. Peninsula Publishing.

Saffman, P.G., 1992. Vortex Dynamics. Cambridge University Press.

Sakamoto, N., Kamiirisa, H., 2018. Prediction of near field propeller cavitation noise by viscous CFD with semi-empirical approach and its validation in model and full scale. Ocean Eng. 168, 41–59.

Seol, H., Jung, B., Suh, J.C., Lee, S., 2002. Prediction of non-cavitating underwater propeller noise. J. Sound Vib. 257 (1), 131–156.

Seol, H., Suh, J.C., Lee, S., 2005. Development of hybrid method for the prediction of underwater propeller noise. J. Sound Vib. 288 (1–2), 345–360.

Sezen, S., Atlar, M., Fitzsimmons, P., 2021a. Prediction of cavitating propeller underwater radiated noise using RANS & DES-based hybrid method. Ships Offshore Struct. 1–13.

Sezen, S., Cosgun, T., Yurtseven, A., Atlar, M., 2021b. Numerical investigation of marine propeller Underwater Radiated Noise using acoustic analogy part 1: The influence of grid resolution. Ocean Eng. 220, 108448.

Sezen, S., Cosgun, T., Yurtseven, A., Atlar, M., 2021c. Numerical investigation of marine propeller underwater radiated noise using acoustic analogy Part 2: The influence of eddy viscosity turbulence models. Ocean Eng. 220, 108353.

Shen, Y.T., Gowing, S., Jessup, S., 2009. Tip vortex cavitation inception scaling for high Reynolds number applications. J. Fluids Eng. 131 (7).

Spence, J., Fischer, R., Bahtiarian, M., Boroditsky, L., Jones, N., Dempsey, R., 2007. Review of existing and future potential treatments for reducing underwater sound from oil and gas industry activities. Noise Control Eng. 07, 07–001.

Takinacı, A.C., Taralp, T., 2013. Prediction and simulation of broadband propeller noise. J. Mar. Sci. Technol. 21 (5), 6.

Testa, C., Ianniello, S., Salvatore, F., Gennaretti, M., 2008. Numerical approaches for hydroacoustic analysis of marine propellers. J. Ship Res. 52 (01), 57–70.

Tong, X.D., Chen, Y., 2020. Random response of highly skewed propeller-shafting system induced by inflow turbulence. Ocean Eng. 195, 106750.

Tong, X.D., Chen, H.Y., Chen, Y., 2021. Low frequency broadband noise radiated by highly skewed propeller ingesting inflow turbulence. J. Sound Vib. 490, 115709.

Usta, O., Korkut, E., 2019. Prediction of cavitation development and cavitation erosion on hydrofoils and propellers by Detached Eddy Simulation. Ocean Eng. 191, 106512.

Vakili, S.V., Ölçer, A.I., Ballini, F., 2020a. The development of a policy framework to mitigate underwater noise pollution from commercial vessels. Mar. Policy 118, 104004.

Vakili, S.V., Ölçer, A.I., Ballini, F., 2020b. The development of a policy framework to mitigate underwater noise pollution from commercial vessels: The role of ports. Mar. Policy 120, 104132.

Valdenazzi, F., Conti, F., Gaggero, S., Vaccaro, C., Grassi, D., Villa, D., 2019. A practical tool for the hydro-acoustic optimization of naval propellers. In: VIII International Conference on Computational Methods in Marine Engineering. CIMNE, pp. 296–308.

Veikonheimo, T., Roivainen, J., Huttunen, T., et al., 2016. Underwater noise of an azipod propulsion unit with heavy ice class. In: Arctic Technology Conference. Offshore Technology Conference.

Vesting, F., Bensow, R.E., 2014. On surrogate methods in propeller optimisation. Ocean Eng. 88, 214–227.

Williams, R., Veirs, S., Veirs, V., Ashe, E., Mastick, N., 2019. Approaches to reduce noise from ships operating in important killer whale habitats. Mar. Pollut. Bull. 139, 459–469.

Wittekind, D.K., 2014. A simple model for the underwater noise source level of ships. J. Ship Prod. Des. 30 (1).

Wittekind, D., Schuster, M., 2016. Propeller cavitation noise and background noise in the sea. Ocean Eng. 120, 116–121.

Wu, Q., Huang, B., Wang, G., Cao, S., Zhu, M., 2018. Numerical modelling of unsteady cavitation and induced noise around a marine propeller. Ocean Eng. 160, 143–155.

Yamada, T., Kawakita, C., 2015. Study on practical CFD for unsteady vortices from trailing edge of propeller blades. Mitsubishi Heavy Ind. Tech. Rev. 52 (4), 56.

Yao, H., Liu, Y., Zhang, H., Zhang, Q., 2021. Comparative study on hydrodynamic performance and induced pressure of new canard tandem propellers and conventional propellers. Ocean Eng. 221, 108566.

Yilmaz, N., Aktas, B., Atlar, M., Fitzsimmons, P.A., Felli, M., 2020. An experimental and numerical investigation of propeller-rudder-hull interaction in the presence of tip vortex cavitation (TVC). Ocean Eng. 216, 108024.